JCI insight

Neuronal DAMPs exacerbate neurodegeneration via astrocytic RIPK3 signaling

Nydia P. Chang, … , Rafiq Huda, Brian P. Daniels

JCI Insight. 2024. https://doi.org/10.1172/jci.insight.177002.

Research In-Press Preview Immunology Neuroscience

Astrocyte activation is a common feature of neurodegenerative diseases. However, the ways in which dying neurons influence the activity of astrocytes is poorly understood. Receptor interacting protein kinase-3 (RIPK3) signaling has recently been described as a key regulator of neuroinflammation, but whether this kinase mediates astrocytic responsiveness to neuronal death has not yet been studied. Here, we used the 1-methyl-4-phenyl-1,2,3,6-tetrahydropyridine (MPTP) model of Parkinson's disease to show that activation of astrocytic RIPK3 drives dopaminergic cell death and axon damage. Transcriptomic profiling revealed that astrocytic RIPK3 promoted gene expression associated with neuroinflammation and movement disorders, and this coincided with significant engagement of damage associated molecular pattern (DAMP) signaling. In mechanistic experiments, we show that factors released from dying neurons signal through receptor for advanced glycation endproducts (RAGE) to induce astrocytic RIPK3 signaling, which conferred inflammatory and neurotoxic functional activity. These findings highlight a mechanism of neuron-glia crosstalk in which neuronal death perpetuates further neurodegeneration by engaging inflammatory astrocyte activation via RIPK3.

Find the latest version:

https://jci.me/177002/pdf

1 Neuronal DAMPs exacerbate neurodegeneration via astrocytic RIPK3 signaling

2

3 Nydia P. Chang[1], Evan M. DaPrano[1], Marissa Lindman[1], Irving Estevez[1], Tsui-Wen Chou[1], Wesley R.

4 Evans[1, 2], Marialaina Nissenbaum[3], Micheal McCourt[1], Diego Alzate[1], Colm Atkins[1], Alexander W.

5 Kusnecov[3], Rafiq Huda[1, 2], and Brian P. Daniels[1*]

6

7 [1] Department of Cell Biology and Neuroscience, Rutgers University, Piscataway, NJ 08854, USA

8 [2] W. M. Keck Center for Collaborative Neuroscience, Rutgers University, Piscataway, NJ 08854, USA

9 [3] Department of Psychology, Rutgers University, Piscataway, NJ 08854, USA

10

11

12 *Correspondence:

13 Brian Daniels

14 604 Allison Road

15 Room B314

16 Piscataway, NJ 08854

17 1-848-445-2709

18 b.daniels@rutgers.edu

19

20 **The authors have declared that no conflicts of interest exist.**

21

22

23 **Abstract**

24 Astrocyte activation is a common feature of neurodegenerative diseases. However, the ways in which
25 dying neurons influence the activity of astrocytes is poorly understood. Receptor interacting protein
26 kinase-3 (RIPK3) signaling has recently been described as a key regulator of neuroinflammation, but
27 whether this kinase mediates astrocytic responsiveness to neuronal death has not yet been studied.
28 Here, we used the 1-methyl-4-phenyl-1,2,3,6-tetrahydropyridine (MPTP) model of Parkinson's disease
29 to show that activation of astrocytic RIPK3 drives dopaminergic cell death and axon damage.
30 Transcriptomic profiling revealed that astrocytic RIPK3 promoted gene expression associated with
31 neuroinflammation and movement disorders, and this coincided with significant engagement of damage
32 associated molecular pattern (DAMP) signaling. In mechanistic experiments, we show that factors
33 released from dying neurons signal through receptor for advanced glycation endproducts (RAGE) to
34 induce astrocytic RIPK3 signaling, which conferred inflammatory and neurotoxic functional activity.
35 These findings highlight a mechanism of neuron-glia crosstalk in which neuronal death perpetuates
36 further neurodegeneration by engaging inflammatory astrocyte activation via RIPK3.

37 **Introduction**

38 Recent work has identified a central role for neuroinflammation in the pathogenesis of
39 neurological disease, including major neurodegenerative disorders such as Alzheimer's and
40 Parkinson's disease (1, 2). Although glial cells are critical regulators of neuroinflammation, activated
41 glia serve complex roles during disease, including both protective and pathogenic functions (3). Among
42 glial cells, astrocytes are the most abundant cell type in the central nervous system (CNS), where they
43 support homeostasis via wide-ranging effects on neurotransmission, neurovascular function, and
44 metabolism (4). However, following an inflammatory insult, astrocytes can enter "reactive" states
45 associated with disease pathogenesis (5). While astrocyte activation is likely highly plastic and context-
46 dependent, it is now widely accepted that astrocytes can take on inflammatory transcriptional states
47 during disease that are associated with the conferral of neurotoxic activity and suppression of normal
48 homeostatic functions (6). Despite this understanding, the molecular mechanisms that govern astrocyte
49 reactivity during neurodegenerative disease, and particularly those factors that most directly exacerbate
50 disease progression, remain poorly understood (7).

51 We and others have recently identified receptor interacting protein kinase-3 (RIPK3) as a key
52 regulator of inflammation in the CNS (8-10). RIPK3 signaling is canonically associated with necroptotic
53 cell death, which is induced via the activation of mixed lineage kinase domain-like protein (MLKL) (11).
54 While RIPK3-dependent necroptosis has been implicated in several neurological disorders, RIPK3 also
55 appears to promote neuroinflammatory processes via necroptosis-independent mechanisms, including
56 the coordination of inflammatory transcription in multiple CNS cell types (12-17). While necroptosis-
57 independent roles for RIPK3 signaling in astrocytes have not been thoroughly studied, we have
58 previously shown that pathogenic α-synuclein fibrils activate RIPK3 signaling in human midbrain
59 astrocyte cultures, resulting in NF-κB-mediated transcriptional activation without inducing astrocytic
60 necroptosis (14). However, whether RIPK3 controls astrocyte transcriptional activation and function in
61 models of neurodegenerative disease in vivo is unknown.

The importance of neuron-glia communication during CNS disease states has also gained significant recognition in recent work (18). A particularly important goal in this area is defining the stimuli that induce inflammatory signaling in the "sterile" setting of neurodegeneration. One potential stimulus underlying inflammatory astrocyte activation during neurodegeneration are factors derived from dead and dying neurons, themselves. These factors include damage-associated molecular patterns (DAMPs), molecules released from damaged cells that serve as endogenous danger signals that elicit potent innate immune activation in neighboring cells (19). DAMP release has been associated with numerous inflammatory diseases, including neurodegenerative disorders (20-23). However, whether and how neuron-derived DAMPs impact astrocyte function during neurodegenerative disease has not been thoroughly studied to date.

Here, we define a new role for RIPK3 signaling in mediating astrocyte activation downstream of neuronal DAMP release. We utilize the 1-methyl-4-phenyl-1,2,3,6-tetrahydropyridine (MPTP) model of Parkinson's disease, in which cell death can be selectively induced in dopaminergic neurons in vivo, to show that induction of neuronal cell death results in RIPK3-dependent astrocyte activation, which in turn exacerbates ongoing neurodegeneration. Transcriptional profiling revealed a robust RIPK3-dependent inflammatory signature in astrocytes exposed to dying neuron-derived factors, and this occurred independently of astrocytic MLKL. Mechanistically, we show that factors released from dying dopaminergic neurons activate receptor for advanced glycation endproducts (RAGE) on midbrain astrocytes. RAGE signaling, in turn, was required for RIPK3 activation, inflammatory transcription, and the conferral of neurotoxic activity in midbrain astrocytes following exposure to neuronal DAMPs. Our findings suggest a feed-forward mechanism that perpetuates neurodegeneration via the DAMP-dependent activation of RIPK3-dependent inflammation and neurotoxicity in astrocytes. These results highlight an important mechanism of neuron-glia crosstalk, with implications for the prevention and treatment of neurodegenerative disease.

87 **Results**

88

89 *Astrocytic RIPK3 signaling promotes neurodegeneration in the MPTP model of Parkinson's disease*

90 To examine the impact of astrocytic RIPK3 signaling in response to neuronal cell death, we
91 subjected mice with astrocyte-specific deletion of *Ripk3* (*Ripk3*$^{fl/fl}$ *Aldh1l1*$^{Cre+}$) and littermate controls to
92 treatment with MPTP, a neurotoxin that selectively induces death in dopaminergic neurons (24, 25). We
93 used the subacute model of MPTP administration, in which mice receive 5 daily doses at 20 mg/kg
94 intraperitoneally (i.p.), followed by downstream analysis as depicted in Figure 1A. MPTP administration
95 resulted in significant loss of tyrosine hydroxylase (TH) immunoreactivity in the substantia nigra pars
96 compacta (SNpc) of control animals, consistent with the depletion of dopaminergic neurons in this
97 region (Figure 1B-C). Strikingly, however, *Ripk3*$^{fl/fl}$ *Aldh1l1*$^{Cre+}$ mice exhibited reduced dopaminergic
98 neuron loss following MPTP treatment, suggesting a role for astrocytic RIPK3 in exacerbating neuronal
99 death in this model. We also observed a significant loss of TH^+ dopaminergic axons in the striatum of
100 control animals (Figure 1D-E), along with increased frequencies of TH^+ axons immunoreactive for
101 SMI32, a marker of axonal degeneration (26-28) (Figure 1F). This phenotype was also greatly
102 ameliorated in *Ripk3*$^{fl/fl}$ *Aldh1l1*$^{Cre+}$ mice. To test whether these differences in dopaminergic neuron loss
103 were associated with differences in motor function, we next subjected mice to the vertical grid maze, a
104 motor task previously shown to be sensitive to perturbations of dopaminergic circuits (29, 30).
105 Strikingly, MPTP-treated control mice exhibited significantly impaired performance in the vertical grid
106 maze (Figure 1G-H), while mice lacking astrocytic *Ripk3* did not. Improvements in dopaminergic neuron
107 loss and motor performance in *Ripk3*$^{fl/fl}$ *Aldh1l1*$^{Cre+}$ mice were not due to differential metabolism of
108 MPTP compared to Cre- littermates, as we observed indistinguishable levels of the toxic metabolite of
109 MPTP (MPP^+) in midbrain homogenates derived from animals of both genotypes (Supplemental Figure
110 1A). We also confirmed that *Ripk3* transcript expression was absent in sorted ACSA2+ astrocytes
111 derived from *Ripk3*$^{fl/fl}$ *Aldh1l1*$^{Cre+}$ mice, while *Ripk3* expression in sorted CD11b+ cells was unchanged

112 (Supplemental Figure 1B-D). Together, these data suggest that astrocytic RIPK3 signaling exacerbates
113 neuronal cell death following a neurotoxic insult.

114

115 *RIPK3 drives inflammatory transcriptional activation but not proliferation in midbrain astrocytes*

116 Given these findings, we next questioned how RIPK3 signaling influences the phenotype of
117 astrocytes in the setting of MPTP administration. Immunohistochemical (IHC) staining of SNpc sections
118 revealed increased GFAP staining in MPTP-treated control animals, consistent with astrocyte
119 activation, and this effect was blocked in *Ripk3*$^{fl/fl}$ *Aldh1l1*$^{Cre+}$ mice (Figure 2A-B). To test whether
120 enhanced GFAP staining indicated proliferative astrogliosis, we performed flow cytometric analysis of
121 astrocytes in the midbrain of MPTP-treated animals, which revealed no differences in GLAST^{+}
122 astrocytes between genotypes (Figure 2C-D). These data suggested that enhanced GFAP staining was
123 not due to increased numbers of astrocytes following MPTP administration, but rather a change in the
124 astrocyte activation status. To test this idea, we performed qRT-PCR analysis of a panel of transcripts
125 that we and others have shown to be associated with neurotoxic astrocyte activation in models of
126 Parkinson's disease (14, 31, 32). We observed upregulation of 10 out of 14 transcripts in our analysis
127 panel in midbrain homogenates derived from MPTP-treated littermate controls, while this activation
128 signature was essentially abolished in *Ripk3*$^{fl/fl}$ *Aldh1l1*$^{Cre+}$ mice (Figure 2E). In contrast, MPTP-treated
129 *Mlkl*$^{-/-}$ mice showed equivalent levels of inflammatory transcript expression in the midbrain
130 (Supplemental Figure 2A). We further confirmed a lack of MLKL phosphorylation in midbrain
131 homogenates of MPTP-treated mice using ELISA, suggesting that MLKL is not activated in this region
132 in the subacute MPTP model (Supplemental Figure 2B). These data suggest that astrocytic RIPK3
133 signaling promotes an inflammatory transcriptional state in the midbrain following MPTP treatment,
134 independently of MLKL and necroptosis.

We next more carefully assessed this idea by using a mouse line expressing RIPK3 fused to two FKBP^{F36V} domains that facilitate enforced oligomerization following treatment with a dimerization drug. This protein is expressed in a cell type-specific manner under the control of a lox-STOP-lox element in the *Rosa26* locus, while the endogenous *Ripk3* locus is left intact. Thus, this mouse line can be used as both a cell type-specific overexpression system while also facilitating forced chemogenetic activation of RIPK3 in cell types of interest in vivo (12, 13, 33). We first questioned whether simple overexpression of RIPK3 in astrocytes would enhance the inflammatory transcriptional signature that occurs following MPTP administration. We observed that 4 neurotoxic astrocyte-associated transcripts exhibited augmented upregulation following MPTP administration in *Ripk3*-2xFV$^{fl/fl}$ *Aldh1l1*$^{Cre+}$ mice, including *Ccl5, Cd14, Cxcl10,* and *Psmb8*, while 2 others exhibited trends towards increased expression that did not reach statistical significance (*Cd109, H2-D1*) (Figure 2F). To assess whether activation of astrocytic RIPK3 was sufficient to induce an inflammatory gene signature, we enforced RIPK3 activation in astrocytes via stereotactic delivery of B/B homodimerizer to the ventral midbrain of *Ripk3*-2xFV$^{fl/fl}$ *Aldh1l1*$^{Cre+}$ mice. B/B homodimerizer binds in a multivalent fashion to the FKBP^{F36V} domains of RIPK3-2xFV proteins, driving their oligomerization, which is sufficient to induce RIPK3 kinase activity in the absence of any other stimulus (34, 35) (Figure 2G-H). Enforced activation of RIPK3 in midbrain astrocytes in vivo resulted in induced expression of several neurotoxic astrocyte-associated transcripts, including *Cd14, Emp1, Gbp2, Lcn2, S100a10,* and *Srgn* (Figure 2I). Together, these data show that activation of RIPK3 in midbrain astrocytes drives their activation and the establishment of an inflammatory transcriptional signature.

Astrocytic RIPK3 signaling has minimal impact on microglial activation in the MPTP model

We next questioned whether the reduced expression of inflammatory genes observed in mice lacking astrocytic RIPK3 was associated with cell non-autonomous effects on other cell types in the setting of MPTP treatment. We thus performed IHC staining for IBA1, a marker of myeloid cells that

160 largely labels microglia in the setting of sterile neurodegeneration (36, 37). This analysis revealed no
161 differences in the overall coverage of IBA1 staining in the midbrain in *Ripk3*$^{fl/fl}$ *Aldh1l1*$^{Cre+}$ mice
162 compared to littermate controls (Figure 3A-B). To assess changes to immune cells more carefully, we
163 next performed flow cytometric analysis of leukocytes derived from the midbrain of MPTP-treated mice.
164 This revealed essentially identical frequencies of CD45^{int} CD11b^{+} F4/80^{+} microglia between genotypes
165 (Figure 3C-D), suggesting a lack of difference in microglial proliferation. Despite this, microglia derived
166 from MPTP-treated *Ripk3*$^{fl/fl}$ *Aldh1l1*$^{Cre+}$ mice exhibited diminished expression of the costimulatory
167 molecule CD80 compared to controls (Figure 3E-F), consistent with a less inflammatory phenotype. We
168 also observed very low frequencies of CD45^{hi} infiltrating peripheral immune cells in the MPTP model
169 (Figure 3C), the overall numbers of which did not differ by genotype (Figure 3G). To more explicitly test
170 which cell types were driving differences in the midbrain transcriptional response in *Ripk3*$^{fl/fl}$ *Aldh1l1*$^{Cre+}$
171 animals, we sorted CD11b+ myeloid cells (primarily microglia, given very low levels of infiltrating
172 leukocytes) and ACSA2+ astrocytes and assessed transcript levels of a subset of highly differentially
173 expressed inflammatory genes identified in our studies using midbrain homogenates. We observed
174 significantly diminished expression of *Cxcl10, Lcn2, Psmb8, and Serping1* in sorted astrocytes but not
175 in sorted microglia derived from MPTP-treated *Ripk3*$^{fl/fl}$ *Aldh1l1*$^{Cre+}$ mice compared to controls (Figure
176 3H-I) These data suggest that astrocytic RIPK3 signaling following MPTP administration likely induces
177 neuroinflammation primarily through cell-intrinsic mechanisms, with only modest cell non-autonomous
178 effects on microglia.

179

180 *Astrocytic RIPK3 activation drives a transcriptomic state associated with inflammation and*
181 *neurodegeneration in the midbrain*

182 To characterize how astrocytic RIPK3 shapes the neuroinflammatory state of the brain more
183 thoroughly in the MPTP model, we also performed bulk RNA sequencing (RNA-seq) of isolated
184 midbrain tissues derived from *Ripk3*$^{fl/fl}$ *Aldh1l1*$^{Cre+}$ and littermate controls. Principle component analysis

185 revealed distinct separation of MPTP-treated control animals along PC1, while MPTP-treated
186 conditional knockouts largely clustered with vehicle-treated animals of both genotypes (Figure 4A).
187 Further analysis revealed a robust transcriptional response to MPTP in midbrain tissues of littermate
188 control animals, including 452 significantly upregulated genes and 145 significantly downregulated
189 genes (Figure 4B) compared to vehicle-treated controls. This transcriptional response was blunted in
190 *Ripk3*$^{fl/fl}$ *Aldh1l1*$^{Cre+}$ mice, which exhibited only 195 significantly upregulated genes and 120 significantly
191 downregulated genes compared to genotype-matched vehicle-treated animals (Figure 4C), suggesting
192 that astrocytic RIPK3 signaling drives a major portion of the tissue-wide transcriptional response to
193 MPTP-induced neuronal cell death. In support of this idea, comparison of differentially expressed genes
194 (DEGs) within MPTP-treated groups revealed 120 genes with significantly higher expression and 252
195 genes with significantly lower expression in conditional knockouts compared to littermate controls
196 (Figure 4D).

197 To better understand the functional relevance of these transcriptomic profiles, we performed
198 Ingenuity Pathway Analysis (IPA) of genes differentially expressed between genotypes in MPTP-
199 treated animals. This revealed significant enrichment of several disease and function terms with
200 relevance to our study, including “Progressive Neurological Disorder,” “Movement Disorders,” and
201 others (Figure 4E). Comparisons of differentially regulated canonical pathways showed significant
202 enrichment of pathways relating to programmed cell death and inflammation, as expected (Figure 4F).
203 Notably, terms related to DAMP signaling were also highly enriched, including signaling by HMGB1 and
204 S100 family proteins, both of which are factors released by dying and damaged cells that induce
205 inflammation. Further analysis revealed significant upregulation of genes associated with astrocyte
206 activation (Figure 4G), consistent with our previous qRT-PCR analysis. Comparisons of individual gene
207 expression profiles for 2 selected IPA terms (Movement Disorders and DAMP signaling) revealed
208 dozens of significant DEGs for both terms, characterized by a mix of both up-and down-regulated gene
209 expression. Together, our RNA-seq analysis reveals a central role for astrocytic RIPK3 in promoting

210 gene expression associated with neurodegeneration and neuroinflammation in the midbrain. Our
211 findings also suggest a strong link between DAMP signaling and RIPK3-dependent neuroinflammation.

212

213 *Secreted factors from dying neurons drive RIPK3-dependent astrocyte activation*

214 Given the strong representation of DAMP signaling in our transcriptomic analysis, we
215 questioned whether factors released from dying neurons were important for driving RIPK3-mediated
216 astrocyte activation. To test this, we treated differentiated SH-SY5Y neuroblastoma cells, a commonly
217 used model of catecholaminergic neurons (38), with the toxic MPTP metabolite MPP^+ (5mM) for 24
218 hours, which resulted in around 50% cell death (Supplemental Figure 3A). We harvested the
219 conditioned media (NCM) from these cells, which contained DAMPs and other factors released from
220 dying SH-SY5Y cells, and added it to primary human midbrain astrocyte cultures at a ratio of 1:1 with
221 normal astrocyte culture media (Figure 5A). NCM-treated astrocytes were also treated with the RIPK3
222 inhibitor GSK872 or DMSO vehicle. qRT-PCR analysis of a panel of top DEGs associated with
223 astrocyte activation identified in our in vivo transcriptomic profiling revealed robust induction of
224 inflammatory gene expression in midbrain astrocyte cultures treated with NCM derived from MPP^+-
225 treated SH-SY5Y cultures, hereafter referred to as MPP^+ NCM (Figure 5B), following 24 hours of
226 stimulation. However, pharmacologic inhibition of RIPK3 signaling in astrocytes largely prevented this
227 effect.

228 After these observations, we recognized that our NCM preparations may have contained debris
229 and floating "corpses" from dead SH-SY5Y cells. To assess whether soluble factors or dead cell-
230 associated material was the primary driver of RIPK3-dependent astrocyte activation in our experiments,
231 we carefully fractionated NCM samples to pellet out cellular material from soluble factors in the media.
232 Application of either clarified supernatant (Figure 5C) or resuspended pellet material (Figure 5D) from
233 MPP^+-treated SH-SY5Y cells to midbrain astrocyte cultures revealed that clarified supernatants

234 stimulated expression of many inflammatory genes in astrocytes in a largely RIPK3-dependent manner.
235 In contrast, pellet-derived material was only minimally stimulatory, and this stimulation was RIPK3-
236 independent. We also confirmed that exposure to residual MPP^+ in NCM was not the primary driver of
237 astrocyte activation, as direct application of MPP^+ to midbrain astrocyte cultures did not result in either
238 cell death or upregulation of inflammatory gene expression (Supplemental Figure 3B-C). As we and
239 others have shown that RIPK3 promotes inflammatory gene expression largely through NFκB activation
240 (14, 33, 39), we also confirmed that clarified MPP^+ NCM supernatants induced NFκB activation in
241 astrocytes in a RIPK3-dependent manner (Supplemental Figure 4A), and that blockade of NFκB
242 signaling with the pharmacologic agent JSH-23 greatly suppressed the stimulatory effect of MPP^+ NCM
243 (Supplemental Figure 4B).

244 We next wanted to confirm that inflammatory gene expression in our system corresponded to a
245 functional readout of astrocyte activation. We thus assessed whether exposure to dying neuron-derived
246 factors would confer neurotoxic activity to astrocytes. We first treated human midbrain astrocytes for 24
247 hours with MPP^+ NCM with or without RIPK3 inhibitor (and respective controls), then washed the cells
248 and replaced the astrocyte medium to remove residual MPP^+. We then cultured astrocytes for an
249 additional 24h and collected their conditioned media (ACM), which was then added to fresh cultures of
250 SH-SY5Y cells at a 1:1 ratio with normal SH-SY5Y media (Figure 5E). We observed that astrocytes
251 maintained transcriptional activation for at least 24 hours following this wash step, confirming that
252 astrocytes remain activated after removal of MPP^+ NCM in this paradigm (Supplemental Figure 5).
253 ACM derived from MPP^+ NCM-treated astrocytes induced around 80% cell death in fresh SH-SY5Y
254 cultures after 24 hours, while this neurotoxic activity was completely abrogated when astrocytic RIPK3
255 signaling was inhibited (Figure 5F). Together, these data show that soluble factors released from dying
256 neuron-like cells are sufficient to induce inflammatory transcription and neurotoxic activity in midbrain
257 astrocytes and that this process requires, to a large degree, cell-intrinsic RIPK3 activity within
258 astrocytes.

259

260 *RIPK3 activation is sufficient to induce astrocyte-mediated killing of primary neurons*

261 While our results using the SH-SY5Y cell line were promising, we next sought to recapitulate
262 these findings with *bona fide* primary neuron cultures. We thus treated primary murine mesencephalic
263 neuron cultures with MPP+ or saline to generate NCM, similar to our previous experiments with SH-
264 SY5Y cells. NCM was applied to primary murine midbrain astrocytes derived from *Ripk3*$^{-/-}$ mice or their
265 *Ripk3*$^{+/-}$ littermates (Figure 6A). Expression profiling revealed greatly enhanced expression of
266 inflammatory genes in MPP+ NCM-treated control astrocytes, while this effect was significantly blunted
267 in astrocytes lacking *Ripk3* expression (Figure 6B). To test whether this RIPK3-dependent gene
268 expression was associated with neurotoxic activity, we generated ACM samples from this paradigm
269 and applied them to fresh cultures of primary mesencephalic neurons (Figure 6C). Primary neurons
270 exposed to the conditioned medium of MPP+ NCM treated *Ripk3*$^{+/-}$ astrocytes exhibited significantly
271 diminished viability, while this effect was lost when astrocytes lacked *Ripk3* expression (Figure 6D). To
272 confirm that treatment with MPP+ NCM was sufficient to drive RIPK3 activation, we utilized primary
273 midbrain astrocyte cultures expressing the chimeric RIPK3-2xFV protein, which contains a FLAG-tag
274 (12, 13), under the *Nestin* promoter (which drives expression in astrocyte cultures derived from
275 neonates) in order to facilitate molecular biological analysis. Treatment of RIPK3-2xFV-expressing
276 midbrain astrocytes with MPP+ NCM resulted in robust RIPK3 activation, as evidenced by the
277 abundance of high molecular weight RIPK3 oligomers in samples subjected to DSS-crosslinking
278 (Figure 6E). To assess whether these complexes interacted with MLKL, we pulled down RIPK3
279 following exposure to NCM using beads coated with anti-FLAG antibodies. While we observed highly
280 efficient pulldown of RIPK3, we saw no evidence of interaction with MLKL in pulldown samples (Figure
281 6F), consistent with the idea that changes to astrocyte activation in our model are not due to MLKL
282 activation and necroptosis. We separately confirmed that MPP+ NCM did not induce cell death in
283 primary midbrain astrocytes, nor did it induce MLKL phosphorylation (Supplemental Figure 6A-B). We

284 also tested whether direct chemogenetic activation of RIPK3 was sufficient to reproduce our phenotype
285 by treating RIPK3-2xFV expressing astrocytes with B/B homodimerizer. This treatment resulted in
286 robust induction of inflammatory gene expression in *Nestin*-Cre$^+$ cultures, but not in cultures lacking
287 transgene expression (*Nestin*-Cre$^-$) (Figure 6G). Finally, we also generated ACM from astrocytes
288 treated in this paradigm (Figure 6H) and tested for neurotoxic activity on primary mesencephalic
289 neurons, which revealed that chemogenetic activation of astrocytic RIPK3 was also sufficient to induce
290 neurotoxicity (Figure 6H). Together, these data support our findings that necroptosis-independent
291 RIPK3 activation is sufficient to drive inflammatory and neurotoxic activity in midbrain astrocytes.

292

293 *DAMP signaling via RAGE drives inflammatory activation in midbrain astrocytes*

294 We next sought to more precisely identify specific DAMP signals that stimulate midbrain
295 astrocyte activation. Our transcriptomic analysis revealed that both HMGB1 and S100 family signaling
296 were highly enriched in an astrocytic RIPK3-dependent manner in the midbrain following MPTP
297 treatment. As both of these DAMPs stimulate a common receptor, RAGE, we assessed whether RAGE
298 was required for astrocyte activation following exposure to MPP$^+$ NCM. We thus treated human
299 midbrain astrocyte cultures with MPP$^+$ or control NCM, along with the RAGE inhibitor FPS-ZM1 for 24
300 hours and performed qRT-PCR profiling (Figure 7A). Blockade of RAGE in astrocytes substantially
301 reduced MPP$^+$ NCM-induced transcriptional activation, effectively preventing upregulation of 6 out of 11
302 astrocyte activation-associated transcripts (Figure 7B). Based on these findings, we confirmed that the
303 RAGE ligand HMGB1 was, in fact, released by SH-SY5Y cells following induction of cell death by MPP$^+$
304 (Figure 7C). We also observed significant accumulation of HMGB1 protein in midbrain homogenates of
305 mice treated with MPTP (Figure 7D), confirming that induction of dopaminergic cell death results in the
306 release of RAGE ligands in vivo. We further confirmed that RAGE ligands drive astrocyte activation in
307 our model by treating midbrain astrocytes with NCM in the presence of HMGB1 neutralizing antibodies,
308 which significantly blunted the transcriptional activation induced by MPP$^+$ NCM (Figure 7E).

309 To assess whether RAGE ligands induced astrocyte activation in a RIPK3-dependent manner,
310 we next treated primary midbrain astrocytes with recombinant DAMPs and profiled gene expression.
311 Strikingly, we observed that stimulation of murine midbrain astrocytes with HMGB1 induced robust
312 transcriptional activation that was blocked in the presence of GSK 872 (Figure 7F). As a complimentary
313 approach, we also generated midbrain astrocyte cultures from *Ripk3*$^{-/-}$ mice (and heterozygous
314 littermate controls) and stimulated with RAGE ligands. Treatment with either HMGB1 (Figure 7G) or
315 S100β (Figure 7H) induced inflammatory transcript expression in control but not *Ripk3*$^{-/-}$ cultures. To
316 confirm that HMGB1 could drive RIPK3-dependent astrocyte activation in vivo, we performed
317 intracerebroventricular (ICV) administration of recombinant HMGB1 in *Ripk3*$^{fl/fl}$ *Aldh1l1*$^{Cre+}$ mice and
318 littermate controls. We then sorted ACSA2+ astrocytes via MACS 24h following HMGB1 treatment.
319 While ICV delivery of HMGB1 robustly induced transcriptional activation in control astrocytes, this effect
320 was significantly blunted in astrocytes lacking *Ripk3* expression (Figure 7I). Together, these data
321 support a model in which dying neurons release DAMPs that induce inflammatory astrocyte activation
322 through activation of astrocytic RAGE, which in turn drives transcriptional activation via RIPK3
323 signaling.

324

325 *Activation of RIPK3 by DAMP signaling drives pathogenic functional changes in midbrain astrocytes*

326 To confirm that the transcriptional effects of DAMP signaling impacted astrocyte function, we
327 collected astrocyte conditioned media (ACM) from astrocytes treated for 24h with MPP$^+$ NCM with or
328 without RAGE inhibitor (and respective controls) and applied the ACM to fresh cultures of SH-SY5Y
329 cells (Figure 8A). ACM derived from MPP$^+$ NCM-treated astrocytes robustly induced cell death in fresh
330 SH-SY5Y cultures, while this neurotoxic activity was completely abrogated when astrocytic RAGE
331 signaling was inhibited (Figure 8B). We also observed conferral of neurotoxic activity following direct
332 stimulation of astrocytes with recombinant DAMPs (Figure 8C), including HMGB1 (Figure 8D) and
333 S100β (Figure 8E). However, this neurotoxic activity was also abrogated when RIPK3 signaling was

334 blocked, further supporting a role for a RAGE-RIPK3 axis in promoting neurotoxic astrocyte activation.
335 This neurotoxic activity was not due to residual recombinant DAMPs in ACM, as direct application of
336 either DAMP ligand to SH-SY5Y cells did not result in cell death (Supplemental Figure 7). As previous
337 work has shown that neurotoxic astrocytes downregulated key homeostatic functions such as
338 phagocytosis (14, 31), we also exposed midbrain astrocyte cultures to labeled debris generated from
339 SH-SY5Y cells and measured phagocytic uptake of debris via flow cytometry (Figure 8F). Direct
340 stimulation of astrocytes with HMGB1 resulted in a significant reduction in uptake of CSFE-labeled
341 debris, while this suppression of phagocytic function was blocked in the presence of a RIPK3 inhibitor
342 (Figure 8G-H). We also observed that MPP^+ NCM similarly reduced astrocytic phagocytosis in a
343 RIPK3-dependent fashion (Figure 8I). These data further support the notion that DAMPs emanating
344 from dying neurons alter astrocytic function via activation of RIPK3 signaling.

345

346 **Discussion**

347 Our study defines a previously unknown role for neuronal DAMPs in promoting neurotoxic
348 astrocyte activation. This effect was mediated by RIPK3-mediated transcriptional activation, an effect
349 that occurred independently of the necroptotic executioner protein MLKL. Mechanistically, we found
350 that astrocytic RAGE signaling was required for astrocyte activation downstream of DAMP exposure,
351 and this RAGE/RIPK3 signaling axis promoted inflammatory transcription and neurotoxic functional
352 activity. Intriguingly, these results suggest that neuronal death, itself, potentiates a feed-forward
353 process of astrocyte activation and further neuronal cell death. These findings highlight an important
354 mechanism of neuron-glia crosstalk in the pathogenesis of neurodegeneration.

355 DAMPs have previously been implicated as drivers of inflammation in a broad variety of
356 disorders, including neurodegeneration, ischemic stroke, autoimmunity, cardiovascular disease, and
357 others (40-46). RAGE ligands, in particular, have been associated with neurodegenerative disease and
358 have been the target of preclinical therapeutic development. For example, S100β levels in serum and
359 cerebrospinal fluid (CSF) has been shown to correlate with disease severity in Parkinson's disease (22,
360 47). Mice deficient in S100β are also resistant to MPTP-driven neurodegeneration (22), consistent with
361 a role for this molecule in perpetuating neuronal cell death. Similarly, antibody-mediated neutralization
362 of HMGB1 has been shown to attenuate glial cell activation and prevent neuron loss in models of both
363 Alzheimer's disease and Parkinson's disease (21, 48). Despite these findings, other groups have also
364 described neuroprotective functions for RAGE ligands (49), including stimulation of neurotrophic growth
365 factor expression in amyotrophic lateral sclerosis (50), suppression of amyloidosis (51), and direct anti-
366 apoptotic effects in neurons (52, 53). These complex effects appear to be highly context-dependent,
367 differing by cell type, disease state, and even DAMP concentration (52, 54, 55). Our data support a
368 pathogenic role for RAGE signaling in the promotion of neurotoxic astrocyte activation.

369 Astrocytes express RAGE and other DAMP sensors, although cell type-specific functions for
370 DAMP signaling in astrocytes have not been thoroughly studied (56). Existing studies suggest that

371 astrocytic RAGE signaling is pathogenic, on balance (57-59). In Huntington's disease, RAGE-positive
372 astrocytes have been shown to have high levels of nuclear NF-κB (58), consistent with a role for this
373 pathway in promoting inflammatory astrocyte activation. Diminished levels of HMGB1 following
374 berberine treatment was also correlated with diminished astrocyte activation in a model of sepsis (60).
375 Astrocytes are also major sources of RAGE ligands, particularly S100β, and much work to date has
376 focused on autocrine RAGE signaling in astrocytes as a result (61-63). We took advantage of the
377 MPTP model, which induces death selectively in neurons but not astrocytes (64), as well as serial
378 culture systems to more directly assess the impact of paracrine RAGE signaling on astrocyte activation
379 and function. Our study suggests that DAMPs released from dying neurons potently induce
380 inflammatory astrocyte activation via RAGE, driving neurotoxic activation and perpetuating further
381 neuronal cell death. These findings identify RAGE as a promising target for modulating astrocytic
382 responses to neuronal cell death during neurodegenerative disease.

383 RIPK3 signaling has previously been shown to drive pathogenic neuroinflammation and
384 neuronal cell death in several models of neurological disorders (14, 15, 65-68). While many studies
385 have reported neuronal necroptosis as a driver of neurodegeneration, we and others have described
386 necroptosis-independent functions for this kinase in the coordination of neuroinflammation (12-17, 69).
387 To date, RIPK3 signaling in astrocytes has received relatively little attention. Our findings here suggest
388 that DAMP signaling activates astrocytic RIPK3 via RAGE signaling, which drives an inflammatory
389 transcriptional program, even in the absence of MLKL. These data suggest that astrocytic RAGE
390 signaling does not induce inflammation via necroptosis, consistent with our prior work showing
391 necroptosis-independent RIPK3 signaling in astrocytes exposed to fibrillar α-synuclein (14).

392 Future work will be needed to define the signaling events that mediate RAGE-dependent RIPK3
393 activation. A recent study demonstrated co-immunoprecipitation of RIPK3 with RAGE in an endothelial
394 cell line following stimulation with TNF-α (70), but the nature of this interaction and whether it happens
395 under natural conditions in vivo remains to be established. While some studies have observed RIPK3

396 activation downstream of HMGB1 (71, 72), these effects may have been mediated by non-RAGE
397 HMGB1 receptors such as TLR4, which is known to stimulate RIPK3 via its adaptor molecule TRIF (73,
398 74). Both RAGE and RIPK3 signaling appear to converge on the potent activation of NF-κB (33, 75-78),
399 which may provide clues concerning their potential molecular interactions. In any event, delineating the
400 molecular events that promote pathogenic astrocyte activation downstream of DAMP signaling will
401 likely be required to effectively target this pathway for future therapeutic development.
402

403 **Methods**

404 **Sex as a biological variable**

405 For in vivo studies using MPTP, only male mice were used in this study as female mice exhibit acute
406 toxicity and high rates of mortality following exposure to MPTP (24). Other in vivo studies, including B/B
407 homodimerizer and HMGB1 injection, were performed in balanced groups of both male and female
408 animals. For in vitro studies, primary cells were pooled from both male and female donors or animals.
409 The SH-SY5Y cell line was originally derived from a female donor. Sexually dimorphic phenotypes were
410 not observed in experiments where the sex of experimental subjects was mixed.

411 **Mouse lines**

412 Mice were bred and housed under specific-pathogen free conditions in Nelson Biological Laboratories
413 at Rutgers University. *Ripk3*$^{-/-}$ and *Ripk3*$^{fl/fl}$ mouse lines were generously provided by Genentech, Inc
414 (San Francisco, CA, USA). *Mlkl*$^{-/-}$ (79) and *Ripk3*-2xFV$^{fl/fl}$ (12) lines were provided by Andrew Oberst
415 (University of Washington, Seattle, WA, USA). *Aldh1l1*-Cre/ERT2 mice were obtained from Jackson
416 Laboratories (Line 031008) and all animals expressing this transgene were treated for five days with 60
417 mg/kg tamoxifen (Sigma-Aldrich, T5648) in sunflower oil (Sigma-Aldrich, S5007) (i.p.) at least one week
418 prior to further experimentation. *Nestin*-Cre mice were obtained from Jackson Laboratories (Line
419 003771). All genotyping was performed in house using ear punch tissue lysed overnight in DirectPCR
420 Lysis Reagent (Viagen, 102-T) and Proteinase K (Sigma, #3115828001). Sequences for genotyping
421 primers are listed in the Supplemental Table S1. PCR bands were visualized on 2% agarose (VWR,
422 97062) in TBE (VWR, E442) and stained in Diamond Nucleic Acid Stain (Promega, H1181). All
423 experiments were performed in 8-12 week old animals, following protocols approved by the Rutgers
424 University Institutional Animal Care and Use Committee (IACUC). All transgenic animal lines were
425 backcrossed for at least 10 generations on a C57BL/6J background.

426 **MPTP model**

427 1-methyl-4-phenyl-1,2,3,6-tetrahydropyridine (MPTP) was administered at 20 mg/kg (i.p.) once per day
428 for five days (80). Animals were harvested three days following the final MPTP injection for gene
429 expression and flow cytometry experiments. Animals were harvested seven days after the last injection
430 for immunofluorescent detection of neurodegeneration, as well as vertical grid maze studies (see
431 Figure 1A). Effective depletion of dopaminergic neurons was assessed via immunostaining for TH, a
432 marker widely used to identify dopamine neurons in models of Parkinson's disease (24, 81).

433 **Tissue collection**

434 Mice were perfused transcardially with ice cold phosphate-buffered saline (PBS) followed by 4%
435 paraformaldehyde (PFA) for IF experiments. Perfused brains were stored in 4% PFA overnight followed
436 by 48 hours in 30% sucrose in PBS. For transcriptional and ELISA studies, mice were perfused with
437 PBS and midbrain and/or striatal tissues were collected and homogenized for downstream analyses.

438 **Cell culture and treatment**

439 Primary human midbrain astrocytes (ScienCell Research Laboratories, Carlsbad, CA, USA) were
440 cultured in astrocyte media (ScienCell, 1801) supplemented with 2% heat-inactivated fetal bovine
441 serum (FBS) (ScienCell, 0010), astrocyte growth supplement (ScienCell, 1852), and
442 penicillin/streptomycin (ScienCell, 0503). Cells from at least two distinct donors were used for all
443 experiments. Human neuroblastoma SH-SY5Y cells (ATCC, CRL-2266) were cultured in DMEM
444 medium (VWR, 0101–0500) supplemented with 10% FBS (Gemini Biosciences, 100–106),
445 nonessential amino acids (Hyclone, SH30138.01), HEPES (Hyclone, 30237.01), penicillin/streptomycin
446 (Gemini Biosciences, 400–110), and amphotericin B antifungal (Gemini Biosciences, 100–104).
447 Differentiation and experimentation occurred in stocks having undergone less than 15 passages. SH-
448 SY5Y neuroblastoma cells were differentiated into mature neuron-like cells by treating with retinoic acid
449 (4 µg/mL; Sigma-Aldrich, R2625) and BDNF (25 ng/mL; Sigma-Aldrich, B3795) in low serum (2%) SH-
450 SY5Y media. Differentiated SH-SY5Y cultures were used for experiments five to seven days post-

451 differentiation. MPP⁺ iodide (Sigma-Aldrich, D048) was formulated in water to a stock concentration of
452 500 mM. Recombinant HMGB1 (R&D Systems, 1690-HMB-050) and S100B (Human: R&D Systems,
453 1820-SB; Mouse: Novus Biologicals, NBP2-53070) were formulated according to manufacturer
454 recommendations. For cell culture experiments, all recombinant DAMPs were used at a final
455 concentration of 100 ng/mL for 24 h before collection of preconditioned media and cell lysates. GSK
456 872 was purchased from Millipore Sigma (530389). FPS-ZM1 was purchased from Sigma-Aldrich
457 (55030). JSH-23 was purchased from Selleck Chem (S7351). All inhibitors were solubilized in DMSO
458 and used at a final concentration of 1 μM (GSK 872 and FPS-ZM1) or 50 μM (JSH-23).

459 **Primary mouse cell isolation and culture**

460 Primary mouse midbrain astrocytes were cultured from dissected midbrain tissues derived from mouse
461 pups on postnatal day three (P3). Tissue was dissociated using Miltenyi Neural Dissociation Kit (T)
462 following manufacturer's instructions (Miltenyi, 130-093-231). Midbrain astrocytes were cultured on
463 fibronectin-coated flasks and non-astrocytic cells were removed via differential adhesion, as previously
464 described (82). Astrocytes were expanded in AM-a medium (ScienCell, 1831) supplemented with 10%
465 FBS, Astrocyte Growth Supplement-animal (ScienCell, 1882) and Penicillin/Streptomycin Solution
466 (ScienCell, 0503). Primary mouse mesencephalic neuron cultures were generated and maintained as
467 described (83, 84). Neurons were cultured for 7 days prior to use in experiments.

468 **Cell viability test**

469 Cell viability was assessed with the CellTiter-Glo Luminescent Cell Viability Assay kit (Promega,
470 G7573), according to the manufacturer's instructions. Luminescence signal was measured with a
471 SpectraMax iD3 plate reader (Molecular Devices).

472 **Phagocytosis assay**

473 Differentiated SH-SY5Y neuronal cells were labeled with BioTracker CSFE Cell Proliferation Kit
474 (Millipore Sigma, SCT110) according to the manufacturer's protocol. Cell death was induced by

475 exposure to TNF-α at 100 ng/mL and cycloheximide (Sigmal-Aldrich, 66-81-9) at 100 μg/mL for 24 h.
476 Labelled cell debris was collected by centrifugation. Unlabeled neuronal debris was used as a staining
477 control. To detect phagocytosis, CSFE-labeled neuronal debris was added to primary midbrain
478 astrocyte cultures at a ratio of 1:100 for 24 h. Excess neuronal debris was washed away with PBS.
479 Astrocytes were then harvested with cold 5 mM EDTA in PBS followed by scraping of adherent cells.
480 Astrocytes were stained with Zombie NIR at 1:1000 in 1XPBS according to the manufacturer's protocol,
481 followed by fixation in 1% PFA. Phagocytosed CSFE signal was detected using a Northern Lights flow
482 cytometer (Cytek). Analysis was performed by FlowJo software (FlowJo LLC).

483 **B/B homodimerizer and stereotactic injection**

484 B/B homodimerizer was purchased from Takara USA Inc. (AP20187) and was formulated according to
485 manufacturer's recommendations. Buprenorphine extended-release (3.25mg/kg) was administered
486 subcutaneously immediately prior to surgery. Mice were anaesthetized with isoflurane (4% induction,
487 1% maintenance) and positioned on a heating pad while the head was fixed for stereotactic injection.
488 Each animal received 500 nL of freshly formulated B/B homodimerizer or vehicle delivered by a glass
489 pipette using a Programmable Nanoject III Nanoliter Injector (Drummond) unilaterally into the right
490 ventral lateral midbrain (relative to bregma: coordinates A/P: -3.00mm, M/L: -1.20mm, D/V: -4.50mm).
491 The scalp was sutured, and animals were allowed to recover for 24 h before transcriptional analyses.
492 For in vitro studies, B/B homodimerizer was used at a final concentration of 100nM.

493 **Quantitative real-time PCR**

494 Total RNA from homogenized midbrain tissues was extracted using Zymo Direct-zol RNA Miniprep kit,
495 following manufacturer's instructions (Zymo, R2051). Total RNA from cultured cells was isolated using
496 Qiagen RNeasy Mini Kit according to the manufacture's protocol (Qiagen, 74106). RNA yield and
497 quality of the samples were assessed using a NanoDrop spectrophotometer. cDNA was then
498 synthesized with qScript cDNA Synthesis Kit (Quantabio, 95047), followed by qRT-PCR with SYBR

499 Green Master Mix (Bio-Rad, 1725275). Cycle threshold (Ct) values were obtained using QuantStudio 5
500 instrument (Applied Biosystems). Delta Ct was calculated as normalized to Ct values of the
501 housekeeping gene 18S ($Ct_{Target} - Ct_{18S} = \Delta Ct$). Z-scores were calculated to graph heatmaps. Primer
502 sequences in our study are listed in Supplemental Table S2.

503 **Immunofluorescence**

504 Brains were cryosectioned at 12 μm per slice and mounted on a charged slide. Following thawing in a
505 humidified chamber, tissues were incubated in blocking solution consisting of 5% goat serum (Gibco,
506 16210) and 0.2% Triton X-100 for one hour at room temperature. Sections were then incubated with
507 primary antibody diluted in blocking solution overnight at 4°C in a humidified chamber. Antibodies used
508 in this study are listed in Supplemental Table 3. Slides were then washed three times with PBS for 15
509 minutes followed by incubation in secondary antibody diluted in blocking solution for one hour at room
510 temperature. Slides were washed three times to remove secondary antibody and were then stained
511 with 4',6-diamindino-2-phenylindole (DAPI; Biotium, 40011) diluted in PBS for 20 minutes at room
512 temperature, followed by another wash. Sections were cover-slipped with Prolong Diamond Antifade
513 Mountant medium (Invitrogen, P36930). Slides were allowed to dry and images were acquired using
514 Airyscan fluorescent confocal microscope (Carl Zeiss, LSM 800).

515 **Flow Cytometry**

516 After perfusing with ice-cold PBS, mouse midbrains were dissected and minced with a blade. Tissues
517 were then further homogenized via 30 minute incubation in pre-warmed digestion buffer consisting of
518 2% FBS, 1% glutamine, 1% non-essential amino acids, 1% penicillin/streptomycin/amphotericin, and
519 1.5% HEPES, with 0.7U/mL collagenase VIII and 50U/mL DNase I on an orbital shaker. Triturated
520 tissue homogenate was then passed through a 70 μm cell strainer and centrifuged at 350*xg* at 4°C for
521 10 minutes to obtain a single-cell suspension. Cell gradient separation was then achieved by
522 resuspending the pellet in 20% bovine-serum albumin (BSA) in DMEM followed by 20 minute

523 centrifugation at 4°C. After removing the myelin layer, the cell gradient was disrupted by inverting in
524 additional FACS buffer that consisted of 1mM EDTA in PBS with 1% BSA. Resuspended cells were
525 then incubated in antibodies for 30 min at 4°C in the dark. Antibodies used in this study are listed in
526 Supplemental Table 3. After washing with cold FACS buffer, cold 1% paraformaldehyde was then used
527 to fix the cells. Data collection and analysis were performed using a Cytek Northern Lights Cytometer
528 and FlowJo software. Data were normalized using standard counting beads (ThermoFisher, #C36950).

529 **Enzyme-linked immunosorbent assay (ELISA)**

530 The following ELISA kits were used according to the manufacturer's instructions: HMBG1 (Novus
531 Biologicals, NBP2-62766), Phospho-MLKL (RayBiotech, PEL-MLKL-S345-1), and Phospho-NFκB p65
532 (ThermoFisher, 85-86082-11).

533 **FLAG Pulldown and Western Blot**

534 Pulldown of FLAG-tagged RIPK3-2xFV protein was performed using a DYKDDDDK Isolation Kit
535 (Miltenyi 130-101-591) according to manufacturer's instructions. DSS crosslinking was performed as
536 described (35) using DSS crosslinking reagent (ThermoFisher A39267). Western blot was performed
537 as described (85) using antibodies against RIPK3 (Cell Signaling 957025), MLKL (Millipore MABC604),
538 and Actin (Sigma-Aldrich SAB3500350).

539 **Liquid chromatography-mass spectrometry (LC-MS)**

540 A single dosage of MPTP (40 mg/kg) was administered for LC-MS analysis of MPP^+ in vivo. Mice were
541 transcardially perfused with ice-cold PBS 90 min after MPTP injection. Whole brain tissues were then
542 isolated and homogenized in CryoMill tubes containing cold 40:40:20 methanol:acetonitrile:water
543 solution with 0.5% Formic Acid. Following a 10 min incubation on ice, tissue homogenates were then
544 centrifuged in the cold room for 10 min for 16,000 *xg*. Supernatants were then transferred to a new
545 collection tube. The final sample was then treated with 15% NH_4HCO_3. LC/MS was performed at the

546 Metabolomics Shared Resource Core Facility at the Rutgers Cancer Institute of New Jersey (New
547 Brunswick, NJ).

548 **Behavioral assessment**

549 The vertical grid motor assessment task was adapted from previous work (29). Briefly, mice were
550 acclimated to the vertical grid apparatus 3 times a day for 2 consecutive days. On each day, each
551 mouse was placed on the inside of the apparatus 3 cm from the top, facing upward, and was allowed to
552 turn around and climb down. The trial was repeated whenever the mouse failed to climb down and/or
553 turn around within 60 seconds. The same trials were repeated on the day following acclimation and
554 video recorded for analysis.

555 **Bulk RNA sequencing**

556 Total RNA from midbrain tissues was extracted and assessed as described above. RNA samples were
557 sent to Azenta (Piscataway, NJ) for library preparation and Next Generation Sequencing. RNA yield
558 and sample quality were assessed with Qubit (Invitrogen) and TapeStation (Agilent). The Illumina
559 HiSeq platform and 2 x 150-bp paired-end reads were used for the RNA sequencing. Initial analysis
560 was processed by Azenta. The quality of raw RNA-seq data (FASTQ) files were evaluated using
561 FASTQC. Sequence reads were trimmed to remove possible adapter sequences and nucleotides with
562 poor quality using Trimmomatic v.0.36. Trimmed reads were then mapped to the mouse reference
563 genome (GRCm38) available on ENSEMBL using the STAR aligner v.2.5.2b. Unique gene hit counts
564 were calculated by using featureCounts from the Subread package v.1.5.2. The gene hit counts table
565 was used for downstream differential expression analysis via DESeq2. Further statistical analysis was
566 performed using R.

567 **Image analysis**

568 To quantify TH^+ and $SMI32^+$ puncta and co-localization, images were processed by Imaris software
569 (Oxford Instruments, Bitplane 9.5). Object based co-localization was used with the “Coloc” feature. For

570 TH$^+$ and SMI32$^+$ particles, the spot detection function was used to define particles by first creating
571 'vesicles' in each channel. Input intensity for threshold was chosen to best represent the signal for both
572 channels. Colocalized particles were defined with the "classification" feature, where the distance
573 between TH$^+$ and SMI32$^+$ particles within 1 μm or less is considered co-localization. The percentage
574 area and mean intensity of GFAP$^+$ and IBA1$^+$ signal were assessed using Fiji (ImageJ) software.

575 **Statistics**

576 Statistical analysis was completed using GraphPad Prism 9 (GraphPad). Normally distributed data
577 were analyzed using appropriate parametric tests: student's t test (2-tailed) or two-way analysis of
578 variance (ANOVA) with Tukey's multiple comparisons test were used to determine significant
579 differences between groups. A p value less than 0.05 was considered statistically significant. All data
580 points represent biological replicates unless otherwise noted.

581 **Study Approval**

582 All animal experiments were performed with approval of the Rutgers University Institutional
583 Animal Care and Use Committee (IACUC).

584 **Availability of data and materials**

585 All data are available upon reasonable request to the corresponding author. Numerical data
586 associated with this study can be found in the Supporting Data Values file. RNA-seq data generated in
587 this study are deposited in NCBI's Gene Expression Omnibus and can be accessed under accession
588 number GSE237891.

589

590

591

592

593

Author Contributions

Conceptualization: NPC, BPD; Investigation: NPC, ED, ML, IE, TC, WRE, MN, MM, DA, CA, BPD; Analysis: NPC, ED, ML, IE, TC, MM, BPD; Resources: AWK, RH, BPD; Writing – Original Draft: NPC, BPD; Writing – Review and Editing: NPC, ED, TC, CA, BPD; Supervision: CA, AWK, RH, BPD; Funding Acquisition: RH, BPD.

Acknowledgements

This work was supported by a research grant from the American Parkinson's Disease Association, NIH R01 NS120895, and startup funds from Rutgers University (all to BPD), as well as R00 MH112855 (to RH). NPC was supported by F31 NS124242. IE was supported by an HHMI Gilliam Fellowship. WRE was supported by T32 AA028254. LC/MS data were generated by the Rutgers Cancer Institute of New Jersey Metabolomics Shared Resource, supported, in part, with funding from NCI-CCSG P30CA072720-5923. The authors thank Drs. Noriko Goldsmith and Jessica Shivas for assistance with confocal imaging in the Human Genetics Institute of New Jersey Imaging Core Facility. We also thank Eric Chiles and Dr. Xiaoyang Su for assistance with LC/MS. We thank Dr. Pingyue Pan for assistance with mesencephalic neuron cultures. Some figure elements were created with Biorender.com.

611 **References**

612 1. Gilhus NE, Deuschl G. Neuroinflammation - a common thread in neurological disorders. *Nat*
613 *Rev Neurol*. Aug 2019;15(8):429-430. doi:10.1038/s41582-019-0227-8
614 2. Boyd RJ, et al. Neuroinflammation represents a common theme amongst genetic and
615 environmental risk factors for Alzheimer and Parkinson diseases. *J Neuroinflammation*. Sep 8
616 2022;19(1):223. doi:10.1186/s12974-022-02584-x
617 3. Giovannoni F, Quintana FJ. The Role of Astrocytes in CNS Inflammation. *Trends Immunol*. Sep
618 2020;41(9):805-819. doi:10.1016/j.it.2020.07.007
619 4. Endo F, et al. Molecular basis of astrocyte diversity and morphology across the CNS in health
620 and disease. *Science*. Nov 4 2022;378(6619):eadc9020. doi:10.1126/science.adc9020
621 5. Patani R, et al. Functional roles of reactive astrocytes in neuroinflammation and
622 neurodegeneration. *Nat Rev Neurol*. Jul 2023;19(7):395-409. doi:10.1038/s41582-023-00822-1
623 6. Escartin C, et al. Reactive astrocyte nomenclature, definitions, and future directions. *Nat*
624 *Neurosci*. Mar 2021;24(3):312-325. doi:10.1038/s41593-020-00783-4
625 7. Brandebura AN, et al. Astrocyte contribution to dysfunction, risk and progression in
626 neurodegenerative disorders. *Nat Rev Neurosci*. Jan 2023;24(1):23-39. doi:10.1038/s41583-022-
627 00641-1
628 8. Angel JP, Daniels BP. Paradoxical roles for programmed cell death signaling during viral
629 infection of the central nervous system. *Curr Opin Neurobiol*. Dec 2022;77:102629.
630 doi:10.1016/j.conb.2022.102629
631 9. Mangalmurti A, Lukens JR. How neurons die in Alzheimer's disease: Implications for
632 neuroinflammation. *Curr Opin Neurobiol*. Aug 2022;75:102575. doi:10.1016/j.conb.2022.102575
633 10. Heckmann BL, et al. Crashing the computer: apoptosis vs. necroptosis in neuroinflammation.
634 *Cell Death Differ*. Jan 2019;26(1):41-52. doi:10.1038/s41418-018-0195-3

635 11. Morgan MJ, Kim YS. Roles of RIPK3 in necroptosis, cell signaling, and disease. *Exp Mol Med*.
636 Oct 2022;54(10):1695-1704. doi:10.1038/s12276-022-00868-z
637 12. Daniels BP, et al. RIPK3 Restricts Viral Pathogenesis via Cell Death-Independent
638 Neuroinflammation. *Cell*. Apr 6 2017;169(2):301-313 e11. doi:10.1016/j.cell.2017.03.011
639 13. Daniels BP, et al. The Nucleotide Sensor ZBP1 and Kinase RIPK3 Induce the Enzyme IRG1 to
640 Promote an Antiviral Metabolic State in Neurons. *Immunity*. Jan 15 2019;50(1):64-76 e4.
641 doi:10.1016/j.immuni.2018.11.017
642 14. Chou TW, et al. Fibrillar alpha-synuclein induces neurotoxic astrocyte activation via RIP kinase
643 signaling and NF-kappaB. *Cell Death Dis*. Jul 31 2021;12(8):756. doi:10.1038/s41419-021-04049-0
644 15. Wu L, et al. Genetic inhibition of RIPK3 ameliorates functional outcome in controlled cortical
645 impact independent of necroptosis. *Cell Death Dis*. Nov 9 2021;12(11):1064. doi:10.1038/s41419-021-
646 04333-z
647 16. Guo H, et al. RIPK3 and caspase 8 collaborate to limit herpes simplex encephalitis. *PLoS*
648 *Pathog*. Sep 2022;18(9):e1010857. doi:10.1371/journal.ppat.1010857
649 17. Preston SP, et al. A necroptosis-independent function of RIPK3 promotes immune dysfunction
650 and prevents control of chronic LCMV infection. *Cell Death Dis*. Feb 15 2023;14(2):123.
651 doi:10.1038/s41419-023-05635-0
652 18. Gleichman AJ, Carmichael ST. Glia in neurodegeneration: Drivers of disease or along for the
653 ride? *Neurobiol Dis*. Aug 2020;142:104957. doi:10.1016/j.nbd.2020.104957
654 19. Gong T, et al. DAMP-sensing receptors in sterile inflammation and inflammatory diseases. *Nat*
655 *Rev Immunol*. Feb 2020;20(2):95-112. doi:10.1038/s41577-019-0215-7
656 20. Venegas C, Heneka MT. Danger-associated molecular patterns in Alzheimer's disease. *J*
657 *Leukoc Biol*. Jan 2017;101(1):87-98. doi:10.1189/jlb.3MR0416-204R
658 21. Sasaki T, et al. Anti-high mobility group box 1 antibody exerts neuroprotection in a rat model of
659 Parkinson's disease. *Exp Neurol*. Jan 2016;275 Pt 1:220-31. doi:10.1016/j.expneurol.2015.11.003

660 22. Sathe K, et al. S100B is increased in Parkinson's disease and ablation protects against MPTP-
661 induced toxicity through the RAGE and TNF-alpha pathway. *Brain*. Nov 2012;135(Pt 11):3336-47.
662 doi:10.1093/brain/aws250
663 23. Kaur J, et al. Intracellular DAMPs in Neurodegeneration and Their Role in Clinical Therapeutics.
664 *Mol Neurobiol*. Jul 2023;60(7):3600-3616. doi:10.1007/s12035-023-03289-9
665 24. Smeyne RJ, Jackson-Lewis V. The MPTP model of Parkinson's disease. *Brain Res Mol Brain*
666 *Res*. Mar 24 2005;134(1):57-66. doi:10.1016/j.molbrainres.2004.09.017
667 25. Munoz-Manchado AB, et al. Chronic and progressive Parkinson's disease MPTP model in adult
668 and aged mice. *J Neurochem*. Jan 2016;136(2):373-87. doi:10.1111/jnc.13409
669 26. Meller D, et al. Transient immunohistochemical labelling of rat retinal axons during Wallerian
670 degeneration by a monoclonal antibody to neurofilaments. *Brain Res*. Jun 13 1994;648(1):162-6.
671 doi:10.1016/0006-8993(94)91917-8
672 27. Yandamuri SS, Lane TE. Imaging Axonal Degeneration and Repair in Preclinical Animal Models
673 of Multiple Sclerosis. *Front Immunol*. 2016;7:189. doi:10.3389/fimmu.2016.00189
674 28. Manivasagam S, et al. Targeting IFN-lambda Signaling Promotes Recovery from Central
675 Nervous System Autoimmunity. *J Immunol*. Mar 15 2022;208(6):1341-1351.
676 doi:10.4049/jimmunol.2101041
677 29. Kim ST, et al. Vertical grid test and modified horizontal grid test are sensitive methods for
678 evaluating motor dysfunctions in the MPTP mouse model of Parkinson's disease. *Brain Res*. Jan 8
679 2010;1306:176-83. doi:10.1016/j.brainres.2009.09.103
680 30. Zhang W, et al. Identification of ADP/ATP Translocase 1 as a Novel Glycoprotein and Its
681 Association with Parkinson's Disease. *Neurochem Res*. Nov 2022;47(11):3355-3368.
682 doi:10.1007/s11064-022-03688-9
683 31. Liddelow SA, et al. Neurotoxic reactive astrocytes are induced by activated microglia. *Nature*.
684 Jan 26 2017;541(7638):481-487. doi:10.1038/nature21029

685 32. Yun SP, et al. Block of A1 astrocyte conversion by microglia is neuroprotective in models of
686 Parkinson's disease. *Nat Med*. Jul 2018;24(7):931-938. doi:10.1038/s41591-018-0051-5
687 33. Snyder AG, et al. Intratumoral activation of the necroptotic pathway components RIPK1 and
688 RIPK3 potentiates antitumor immunity. *Sci Immunol*. Jun 21
689 2019;4(36)doi:10.1126/sciimmunol.aaw2004
690 34. Orozco SL, et al. RIPK3 Activation Leads to Cytokine Synthesis that Continues after Loss of
691 Cell Membrane Integrity. *Cell Rep*. Aug 27 2019;28(9):2275-2287 e5. doi:10.1016/j.celrep.2019.07.077
692 35. Orozco S, et al. RIPK1 both positively and negatively regulates RIPK3 oligomerization and
693 necroptosis. *Cell Death Differ*. Oct 2014;21(10):1511-21. doi:10.1038/cdd.2014.76
694 36. Lier J, et al. Beyond Activation: Characterizing Microglial Functional Phenotypes. *Cells*. Aug 28
695 2021;10(9)doi:10.3390/cells10092236
696 37. Kenkhuis B, et al. Co-expression patterns of microglia markers Iba1, TMEM119 and P2RY12 in
697 Alzheimer's disease. *Neurobiol Dis*. Jun 1 2022;167:105684. doi:10.1016/j.nbd.2022.105684
698 38. Xicoy H, et al. The SH-SY5Y cell line in Parkinson's disease research: a systematic review. *Mol*
699 *Neurodegener*. Jan 24 2017;12(1):10. doi:10.1186/s13024-017-0149-0
700 39. Najjar M, et al. RIPK1 and RIPK3 Kinases Promote Cell-Death-Independent Inflammation by
701 Toll-like Receptor 4. *Immunity*. Jul 19 2016;45(1):46-59. doi:10.1016/j.immuni.2016.06.007
702 40. Fischer S, et al. Self-extracellular RNA promotes pro-inflammatory response of astrocytes to
703 exogenous and endogenous danger signals. *J Neuroinflammation*. Nov 2 2021;18(1):252.
704 doi:10.1186/s12974-021-02286-w
705 41. Festoff BW, et al. HMGB1 and thrombin mediate the blood-brain barrier dysfunction acting as
706 biomarkers of neuroinflammation and progression to neurodegeneration in Alzheimer's disease. *J*
707 *Neuroinflammation*. Aug 24 2016;13(1):194. doi:10.1186/s12974-016-0670-z
708 42. Banjara M, Ghosh C. Sterile Neuroinflammation and Strategies for Therapeutic Intervention. *Int*
709 *J Inflam*. 2017;2017:8385961. doi:10.1155/2017/8385961

710 43. Silvis MJM, et al. Damage-Associated Molecular Patterns in Myocardial Infarction and Heart
711 Transplantation: The Road to Translational Success. *Front Immunol*. 2020;11:599511.
712 doi:10.3389/fimmu.2020.599511
713 44. Tumburu L, et al. Circulating mitochondrial DNA is a proinflammatory DAMP in sickle cell
714 disease. *Blood*. Jun 3 2021;137(22):3116-3126. doi:10.1182/blood.2020009063
715 45. Santilli F, et al. Soluble forms of RAGE in human diseases: clinical and therapeutical
716 implications. *Curr Med Chem*. 2009;16(8):940-52. doi:10.2174/092986709787581888
717 46. Goldstein RS, et al. Elevated high-mobility group box 1 levels in patients with cerebral and
718 myocardial ischemia. *Shock*. Jun 2006;25(6):571-4. doi:10.1097/01.shk.0000209540.99176.72
719 47. Teismann P, et al. Receptor for advanced glycation endproducts (RAGE) deficiency protects
720 against MPTP toxicity. *Neurobiol Aging*. Oct 2012;33(10):2478-90.
721 doi:10.1016/j.neurobiolaging.2011.12.006
722 48. Kong ZH, et al. The Oral Pretreatment of Glycyrrhizin Prevents Surgery-Induced Cognitive
723 Impairment in Aged Mice by Reducing Neuroinflammation and Alzheimer's-Related Pathology via
724 HMGB1 Inhibition. *J Mol Neurosci*. Dec 2017;63(3-4):385-395. doi:10.1007/s12031-017-0989-7
725 49. Langeh U, Singh S. Targeting S100B Protein as a Surrogate Biomarker and its Role in Various
726 Neurological Disorders. *Curr Neuropharmacol*. 2021;19(2):265-277.
727 doi:10.2174/1570159X18666200729100427
728 50. Brambilla L, et al. Dysregulation of Astrocytic HMGB1 Signaling in Amyotrophic Lateral
729 Sclerosis. *Front Neurosci*. 2018;12:622. doi:10.3389/fnins.2018.00622
730 51. Cristovao JS, et al. The neuronal S100B protein is a calcium-tuned suppressor of amyloid-beta
731 aggregation. *Sci Adv*. Jun 2018;4(6):eaaq1702. doi:10.1126/sciadv.aaq1702
732 52. Huttunen HJ, et al. Coregulation of neurite outgrowth and cell survival by amphoterin and S100
733 proteins through receptor for advanced glycation end products (RAGE) activation. *J Biol Chem*. Dec 22
734 2000;275(51):40096-105. doi:10.1074/jbc.M006993200

735 53. Druse MJ, et al. S100B-mediated protection against the pro-apoptotic effects of ethanol on fetal
736 rhombencephalic neurons. *Brain Res*. May 30 2007;1150:46-54. doi:10.1016/j.brainres.2007.02.092
737 54. Businaro R, et al. S100B protects LAN-5 neuroblastoma cells against Abeta amyloid-induced
738 neurotoxicity via RAGE engagement at low doses but increases Abeta amyloid neurotoxicity at high
739 doses. *J Neurosci Res*. Apr 2006;83(5):897-906. doi:10.1002/jnr.20785
740 55. Sorci G, et al. S100B Protein, A Damage-Associated Molecular Pattern Protein in the Brain and
741 Heart, and Beyond. *Cardiovasc Psychiatry Neurol*. 2010;2010doi:10.1155/2010/656481
742 56. Juranek J, et al. Role of RAGE in the Pathogenesis of Neurological Disorders. *Neurosci Bull*.
743 Oct 2022;38(10):1248-1262. doi:10.1007/s12264-022-00878-x
744 57. Song J, et al. Receptor for advanced glycation end products (RAGE) and its ligands: focus on
745 spinal cord injury. *Int J Mol Sci*. Jul 25 2014;15(8):13172-91. doi:10.3390/ijms150813172
746 58. Kim J, et al. The RAGE receptor and its ligands are highly expressed in astrocytes in a grade-
747 dependant manner in the striatum and subependymal layer in Huntington's disease. *J Neurochem*. Sep
748 2015;134(5):927-42. doi:10.1111/jnc.13178
749 59. Serrano A, et al. The Astrocytic S100B Protein with Its Receptor RAGE Is Aberrantly Expressed
750 in SOD1(G93A) Models, and Its Inhibition Decreases the Expression of Proinflammatory Genes.
751 *Mediators Inflamm*. 2017;2017:1626204. doi:10.1155/2017/1626204
752 60. Shi J, et al. Blocking HMGB1/RAGE Signaling by Berberine Alleviates A1 Astrocyte and
753 Attenuates Sepsis-Associated Encephalopathy. *Front Pharmacol*. 2021;12:760186.
754 doi:10.3389/fphar.2021.760186
755 61. Ponath G, et al. Autocrine S100B effects on astrocytes are mediated via RAGE. *J
756 Neuroimmunol*. Mar 2007;184(1-2):214-22. doi:10.1016/j.jneuroim.2006.12.011
757 62. Villarreal A, et al. S100B protein activates a RAGE-dependent autocrine loop in astrocytes:
758 implications for its role in the propagation of reactive gliosis. *J Neurochem*. Oct 2014;131(2):190-205.
759 doi:10.1111/jnc.12790

760 63. Ding S, et al. Autocrine S100B in astrocytes promotes VEGF-dependent inflammation and
761 oxidative stress and causes impaired neuroprotection. *Cell Biol Toxicol*. Nov 18
762 2021;doi:10.1007/s10565-021-09674-1
763 64. Przedborski S, et al. The parkinsonian toxin 1-methyl-4-phenyl-1,2,3,6-tetrahydropyridine
764 (MPTP): a technical review of its utility and safety. *J Neurochem*. Mar 2001;76(5):1265-74.
765 doi:10.1046/j.1471-4159.2001.00183.x
766 65. Lin QS, et al. RIP1/RIP3/MLKL mediates dopaminergic neuron necroptosis in a mouse model of
767 Parkinson disease. *Lab Invest*. Mar 2020;100(3):503-511. doi:10.1038/s41374-019-0319-5
768 66. Dionisio PA, et al. Ablation of RIP3 protects from dopaminergic neurodegeneration in
769 experimental Parkinson's disease. *Cell Death Dis*. Nov 5 2019;10(11):840. doi:10.1038/s41419-019-
770 2078-z
771 67. Wehn AC, et al. RIPK1 or RIPK3 deletion prevents progressive neuronal cell death and
772 improves memory function after traumatic brain injury. *Acta Neuropathol Commun*. Aug 17
773 2021;9(1):138. doi:10.1186/s40478-021-01236-0
774 68. Ito Y, et al. RIPK1 mediates axonal degeneration by promoting inflammation and necroptosis in
775 ALS. *Science*. Aug 5 2016;353(6299):603-8. doi:10.1126/science.aaf6803
776 69. Cervantes PW, et al. RIPK3 Facilitates Host Resistance to Oral Toxoplasma gondii Infection.
777 *Infect Immun*. Apr 16 2021;89(5)doi:10.1128/IAI.00021-21
778 70. Faust H, et al. RAGE interacts with the necroptotic protein RIPK3 and mediates transfusion-
779 induced danger signal release. *Vox Sang*. Nov 2020;115(8):729-734. doi:10.1111/vox.12946
780 71. Boytard L, et al. Lung-derived HMGB1 is detrimental for vascular remodeling of metabolically
781 imbalanced arterial macrophages. *Nat Commun*. Aug 27 2020;11(1):4311. doi:10.1038/s41467-020-
782 18088-2
783 72. Wen S, et al. HMGB1-associated necroptosis and Kupffer cells M1 polarization underlies
784 remote liver injury induced by intestinal ischemia/reperfusion in rats. *FASEB J*. Mar 2020;34(3):4384-
785 4402. doi:10.1096/fj.201900817R

786 73. Minsart C, et al. New insights in acetaminophen toxicity: HMGB1 contributes by itself to amplify
787 hepatocyte necrosis in vitro through the TLR4-TRIF-RIPK3 axis. *Sci Rep*. Mar 27 2020;10(1):5557.
788 doi:10.1038/s41598-020-61270-1
789 74. Meng R, et al. High mobility group box 1 enables bacterial lipids to trigger receptor-interacting
790 protein kinase 3 (RIPK3)-mediated necroptosis and apoptosis in mice. *J Biol Chem*. May 31
791 2019;294(22):8872-8884. doi:10.1074/jbc.RA118.007040
792 75. Sparvero LJ, et al. RAGE (Receptor for Advanced Glycation Endproducts), RAGE ligands, and
793 their role in cancer and inflammation. *J Transl Med*. Mar 17 2009;7:17. doi:10.1186/1479-5876-7-17
794 76. Kierdorf K, Fritz G. RAGE regulation and signaling in inflammation and beyond. *J Leukoc Biol*.
795 Jul 2013;94(1):55-68. doi:10.1189/jlb.1012519
796 77. Lee KJ, et al. Advanced glycation end products promote triple negative breast cancer cells via
797 ERK and NF-kappaB pathway. *Biochem Biophys Res Commun*. Jan 15 2018;495(3):2195-2201.
798 doi:10.1016/j.bbrc.2017.11.182
799 78. Yu PW, et al. Identification of RIP3, a RIP-like kinase that activates apoptosis and NFkappaB.
800 *Curr Biol*. May 20 1999;9(10):539-42. doi:10.1016/s0960-9822(99)80239-5
801 79. Murphy JM, et al. The pseudokinase MLKL mediates necroptosis via a molecular switch
802 mechanism. *Immunity*. Sep 19 2013;39(3):443-53. doi:10.1016/j.immuni.2013.06.018
803 80. Jackson-Lewis V, Przedborski S. Protocol for the MPTP mouse model of Parkinson's disease.
804 *Nat Protoc*. 2007;2(1):141-51. doi:10.1038/nprot.2006.342
805 81. Pingale T, Gupta GL. Classic and evolving animal models in Parkinson's disease. *Pharmacol*
806 *Biochem Behav*. Dec 2020;199:173060. doi:10.1016/j.pbb.2020.173060
807 82. Daniels BP, et al. Regional astrocyte IFN signaling restricts pathogenesis during neurotropic
808 viral infection. *J Clin Invest*. Mar 1 2017;127(3):843-856. doi:10.1172/JCI88720
809 83. Zhu X, et al. Synaptojanin1 Modifies Endolysosomal Parameters in Cultured Ventral Midbrain
810 Neurons. *eNeuro*. May 2023;10(5)doi:10.1523/ENEURO.0426-22.2023

811 84. Saenz J, et al. Cocaine-regulated trafficking of dopamine transporters in cultured neurons
812 revealed by a pH sensitive reporter. *iScience*. Jan 20 2023;26(1):105782.
813 doi:10.1016/j.isci.2022.105782
814 85. Daniels BP, et al. Viral pathogen-associated molecular patterns regulate blood-brain barrier
815 integrity via competing innate cytokine signals. *mBio*. Aug 26 2014;5(5):e01476-14.
816 doi:10.1128/mBio.01476-14

817

818

819

820

821

822 **Figure Legends**

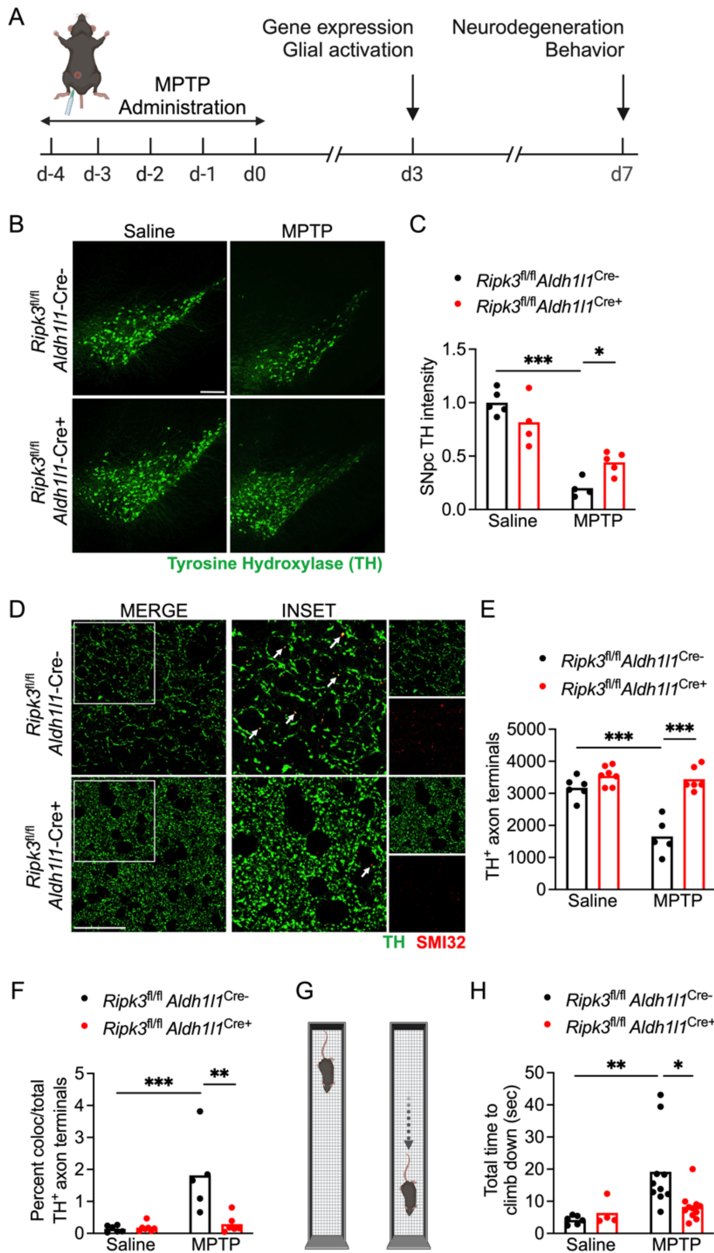

Figure 1. *Astrocytic RIPK3 signaling promotes neurodegeneration in the MPTP model of Parkinson's disease.* **(A)** Schematic diagram showing treatment paradigm for the subacute MPTP model with selected experimental endpoints used in this study. **(B-C)** IHC analysis of tyrosine hydroxylase (TH) staining in the substantia nigra pars compacta (SNpc) in indicated genotypes 7 days following either saline or MPTP treatment (scale bar = 200 μm). **(D-F)** IHC analysis of TH^+ axons with colabeling with the damaged axon marker SMI-32 in the striatum in indicated genotypes 7 days following either saline or MPTP treatment (scale bar = 20 μm). **(G)** Schematic diagram for the vertical grid test. **(H)** Behavioral performance in the vertical

842 grid test 7 days after injection with MPTP or saline. N= 4-5 mice/group **(B-C)**, 5-7 mice/group **(D-F)**, 4-

843 11 mice/group **(H)**. All comparisons via 2-way ANOVA with Sidak's multiple comparison test. $*p<0.05$,

844 $**p < 0.01$, $***p < 0.001$. **(A, G)** were created with Biorender.com.

845

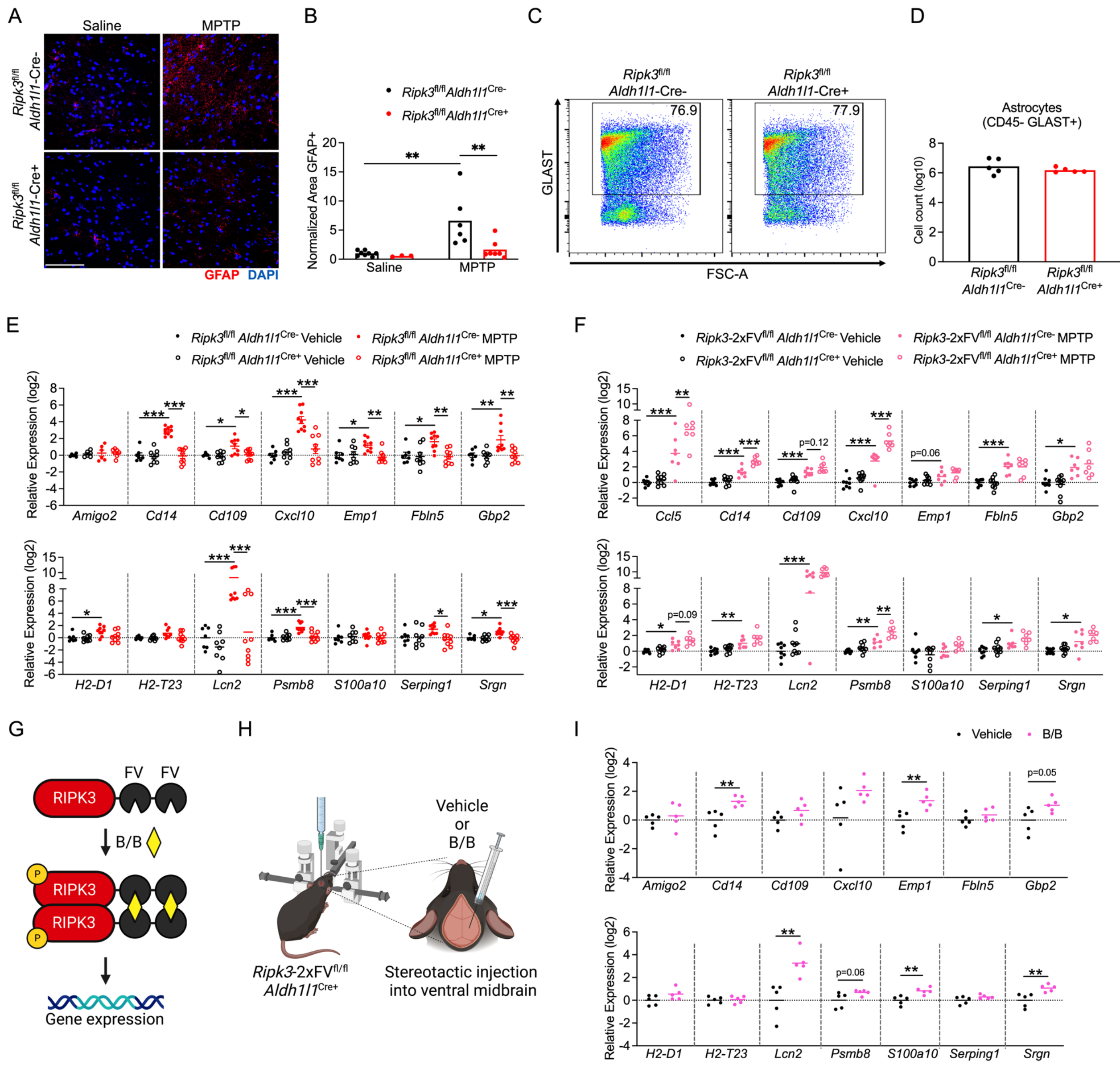

846 **Figure 2. *RIPK3 drives inflammatory transcriptional activation but not proliferation in***
847 ***midbrain astrocytes.*** **(A-B)** IHC analysis of GFAP staining in the substantia nigra pars compacta
848 (SNpc) in indicated genotypes 3 days post-MPTP treatment (scale bar = 200 μm). **(C-D)** Flow
849 cytometric analysis of GLAST+ astrocytes in midbrain homogenates derived from indicated genotypes
850 3 days post-MPTP treatment. **(E-F)** qRT-PCR analysis of indicated genes in midbrain homogenates
851 derived from astrocyte-specific *Ripk3* knockouts **(E)** or astrocyte-specific *Ripk3* overexpressing **(F)** mice
852 3 days post-MPTP treatment. **(G-H)** Schematic of inducible RIPK3 activation system **(G)** and
853 stereotactic delivery of dimerization drug into the ventral midbrain **(H)**. **(I)** qRT-PCR analysis of

854 indicated genes in midbrain homogenates derived from *Ripk3*-2xFV$^{fl/fl}$ *Aldh1l1*-Cre+ mice 24 hours

855 following administration of B/B homodimerizer or vehicle control. N= 3-8 mice/group **(A-B)**, 5

856 mice/group **(C-D)**, 6-9 mice/group **(E)**, 7-8 mice/group **(F)**, 5 mice/group **(I)**. Comparisons via 2-tailed t

857 test **(D)** or 2-way ANOVA with Sidak's multiple comparison test **(B,E,F,I)**. *p<0.05, **p < 0.01, ***p <

858 0.001. **(G, H)** were created with Biorender.com.

859

860

861

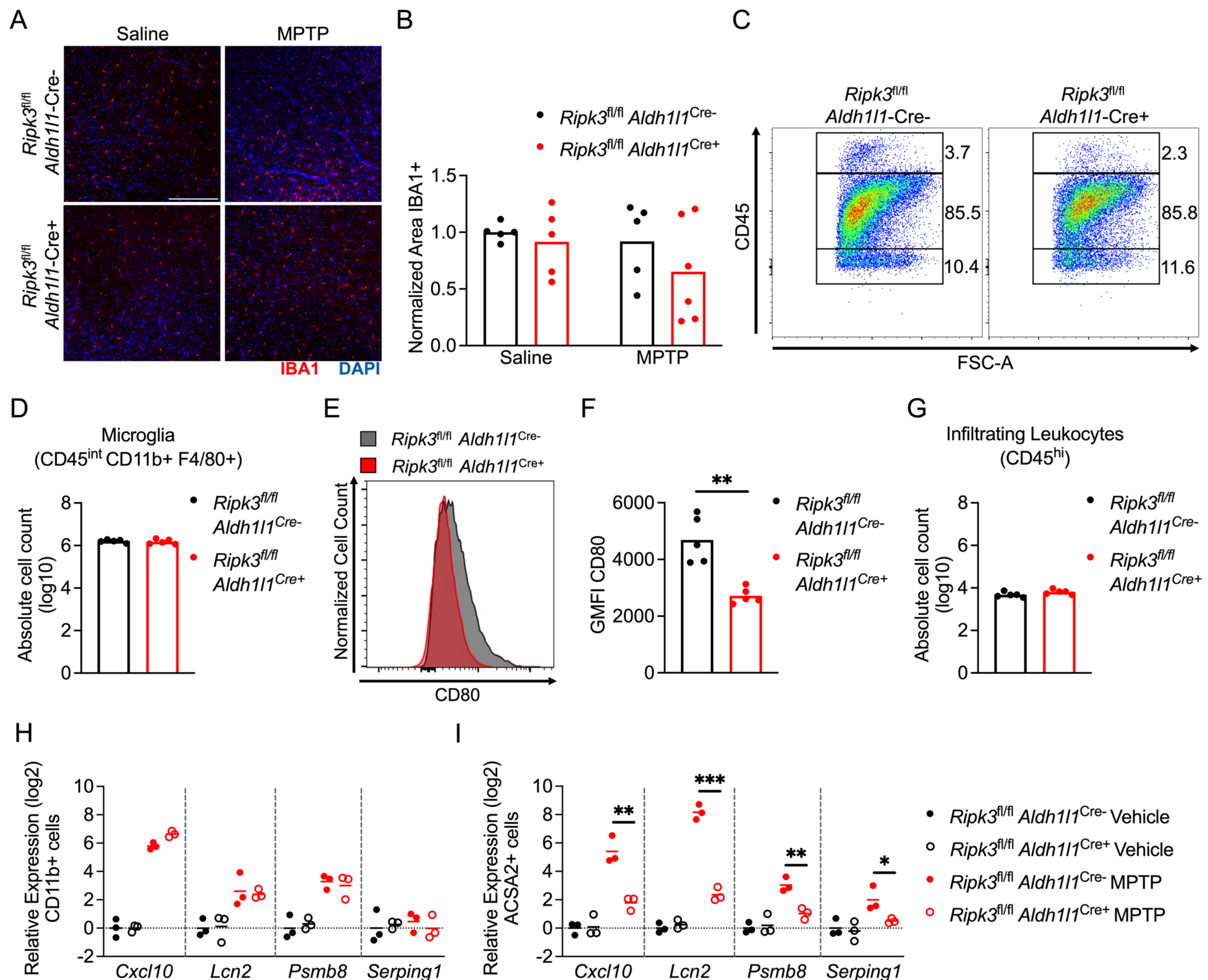

862 **Figure 3. *Astrocytic RIPK3 signaling has minimal impact on microglial activation in the MPTP*
863 *model.* (A-B)** IHC analysis of IBA1 staining in the substantia nigra pars compacta (SNpc) in indicated
864 genotypes 3 days post-MPTP treatment (scale bar = 200 μm). **(C)** Representative flow cytometric plot
865 depicting leukocyte populations in midbrain homogenates derived from indicated genotypes 3 days
866 post-MPTP treatment. **(D)** Quantification of absolute numbers of microglia derived from flow cytometric
867 analysis. **(E-F)** Representative histogram **(E)** and quantification of geometric mean fluorescence
868 intensity (GMFI) **(F)** derived from analysis of CD80 expression on microglial populations in **(D)**. **(G)**
869 Quantification of absolute numbers of $CD45^{hi}$ leukocytes derived from flow cytometric analysis. **(H-I)**
870 qRT-PCR analysis of indicated genes in sorted microglia **(H)** or astrocytes **(I)** derived from astrocyte-

871 specific *Ripk3* knockout mice 3 days post-MPTP treatment. N= 5-6 mice/group **(A-B)**, 5 mice/group **(C-**
872 **G)**, 3 mice/group **(H-I)**. Comparisons via 2-tailed t test **(D,F,G)** or 2-way ANOVA with Sidak's multiple
873 comparison test **(B,H,I)**. *$p<0.05$, **$p < 0.01$, ***$p < 0.001$.

874

875

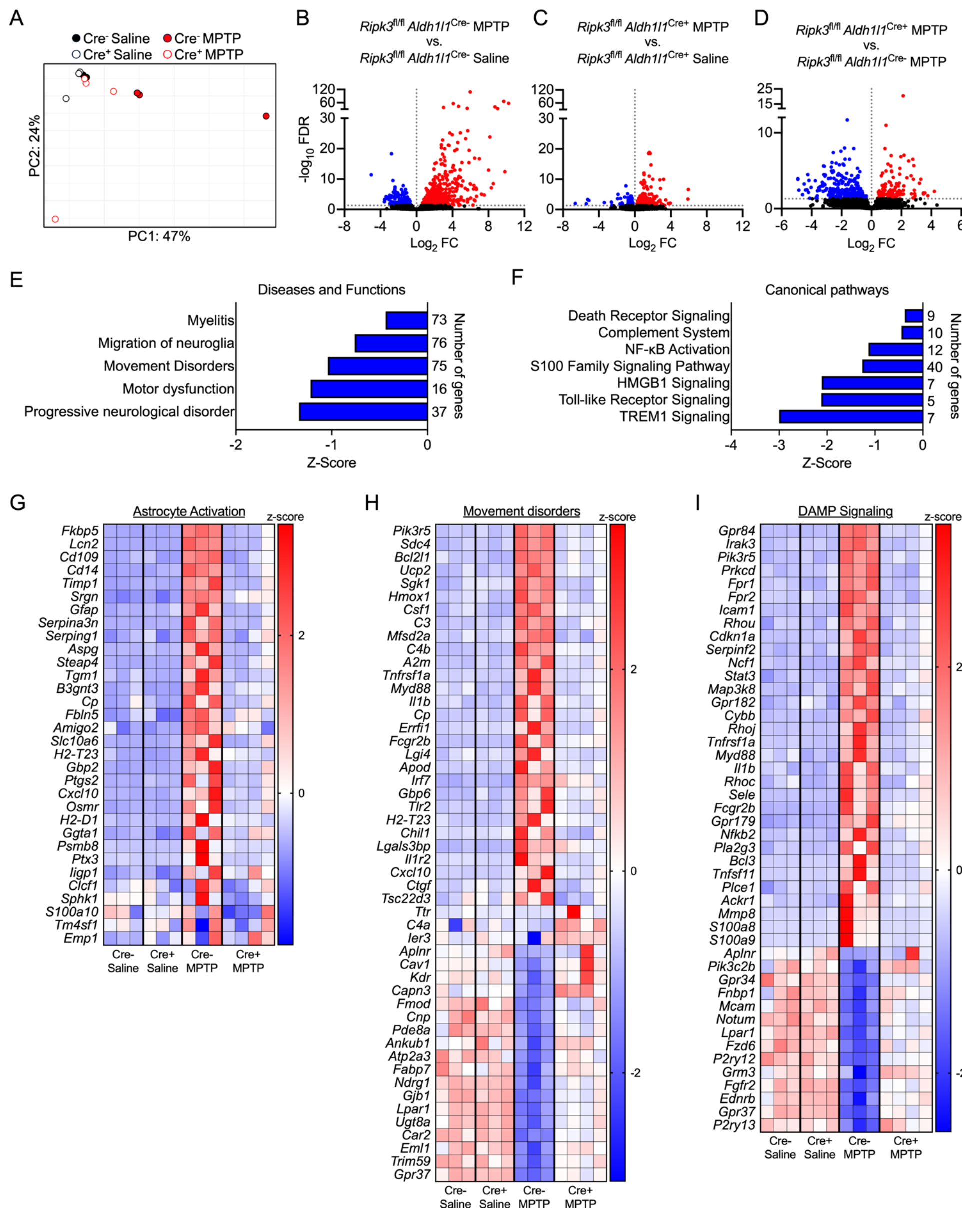

876

877 **Figure 4. *Astrocytic RIPK3 activation drives a transcriptomic state associated with inflammation*
878 *and neurodegeneration in the midbrain.* (A-I)** Midbrains were harvested from mice of indicated
879 genotypes 3 days post-treatment with MPTP or saline and subjected to bulk RNA-seq. (A) Principal
880 component analysis demonstrating separation of treatment groups and genotypes in the RNA-seq
881 dataset. (B-D) Volcano plots showing differentially expressed genes derived from indicated
882 comparisons. Data points in red are genes exhibiting upregulated expression, while those in blue

883 exhibit downregulated expression. Genes with an FDR <0.05 were considered significant. (E-F)

884 Selected significantly enriched disease and function terms (E) or canonical pathways (F) derived from

885 Ingenuity Pathway Analysis comparing Cre- vs. Cre+ MPTP-treated groups. (G-I) Heatmaps showing

886 significantly differentially expressed genes for selected pathways. N= 3-4 mice/group in all panels.

887

888

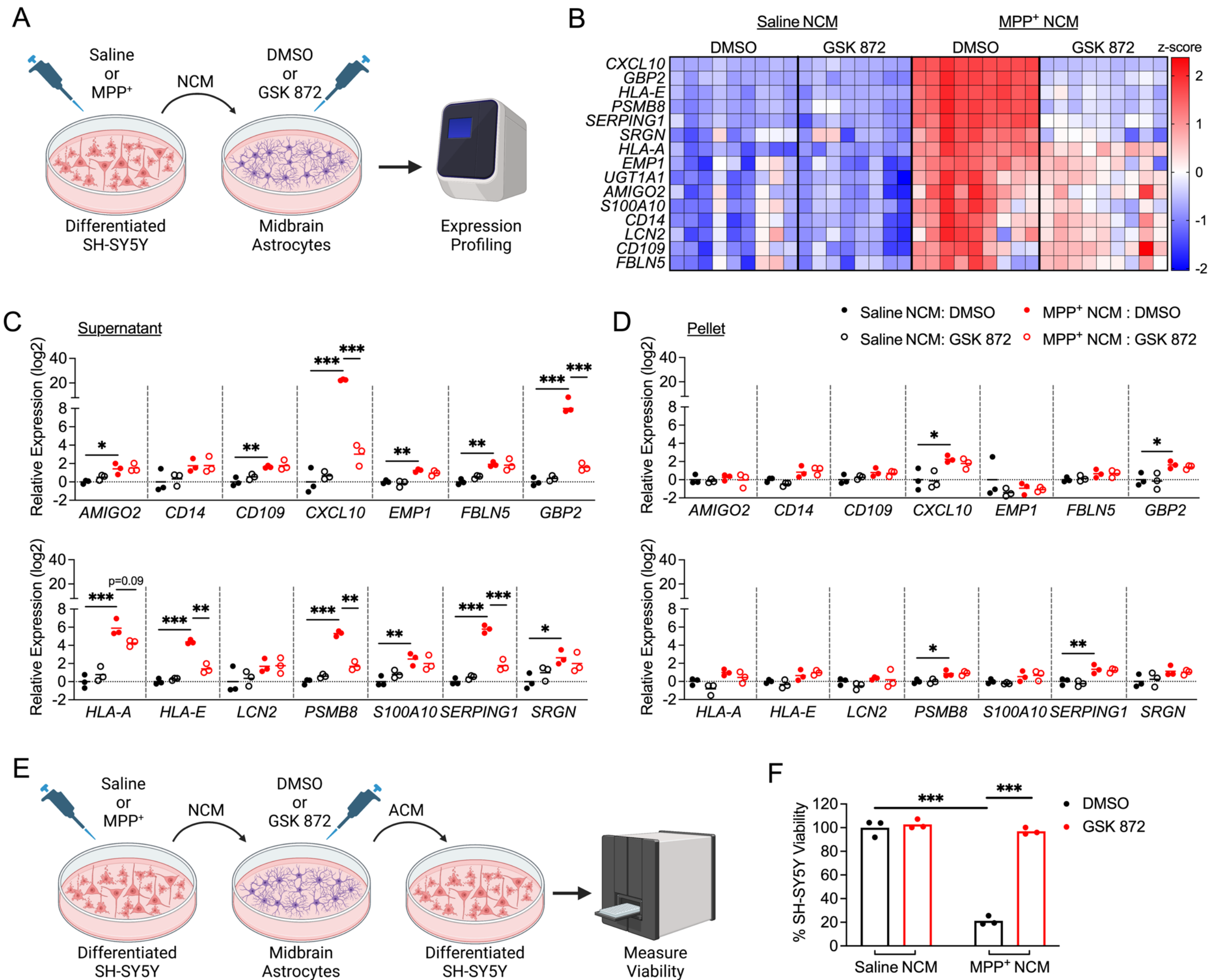

889 **Figure 5. *Secreted factors from dying neurons drive RIPK3-dependent astrocyte activation.* (A)**
890 Schematic of experimental design for DAMP transfer experiments. Differentiated SH-SY5Y cells were
891 treated with MPP^+ or saline for 24h and media (NCM) was then transferred to cultures of primary
892 human midbrain astrocytes. Astrocytes were treated with NCM in the presence of GSK 872 or control
893 for 24h prior to qRT-PCR profiling. **(B)** Heatmap showing expression of astrocyte activation-associated
894 genes in astrocyte cultures treated as in **(A)**. **(C-D)** qRT-PCR profiling of indicated genes in astrocytes
895 treated for 24h with clarified NCM supernatants **(C)** or pelleted SH-SY5Y debris **(D). (E)** Schematic of
896 experimental design for neurotoxicity assay. Astrocytes were treated with NCM as in **(A)** for 24h.
897 Astrocytes were then washed and media replaced for another 24h. This new astrocyte conditioned

medium (ACM) was then transferred to fresh SH-SY5Y cells for cell viability measurement. **(F)** Cell Titer Glo analysis of SH-SY5Y viability 24h following treatment with ACM derived from indicated conditions. N= 9 cultures/group **(A)**, 3 cultures/group **(C, D, F)**. All comparisons via 2-way ANOVA with Sidak's multiple comparison test. $^{*}p<0.05$, $^{**}p < 0.01$, $^{***}p < 0.001$. **(A, E)** were created with Biorender.com.

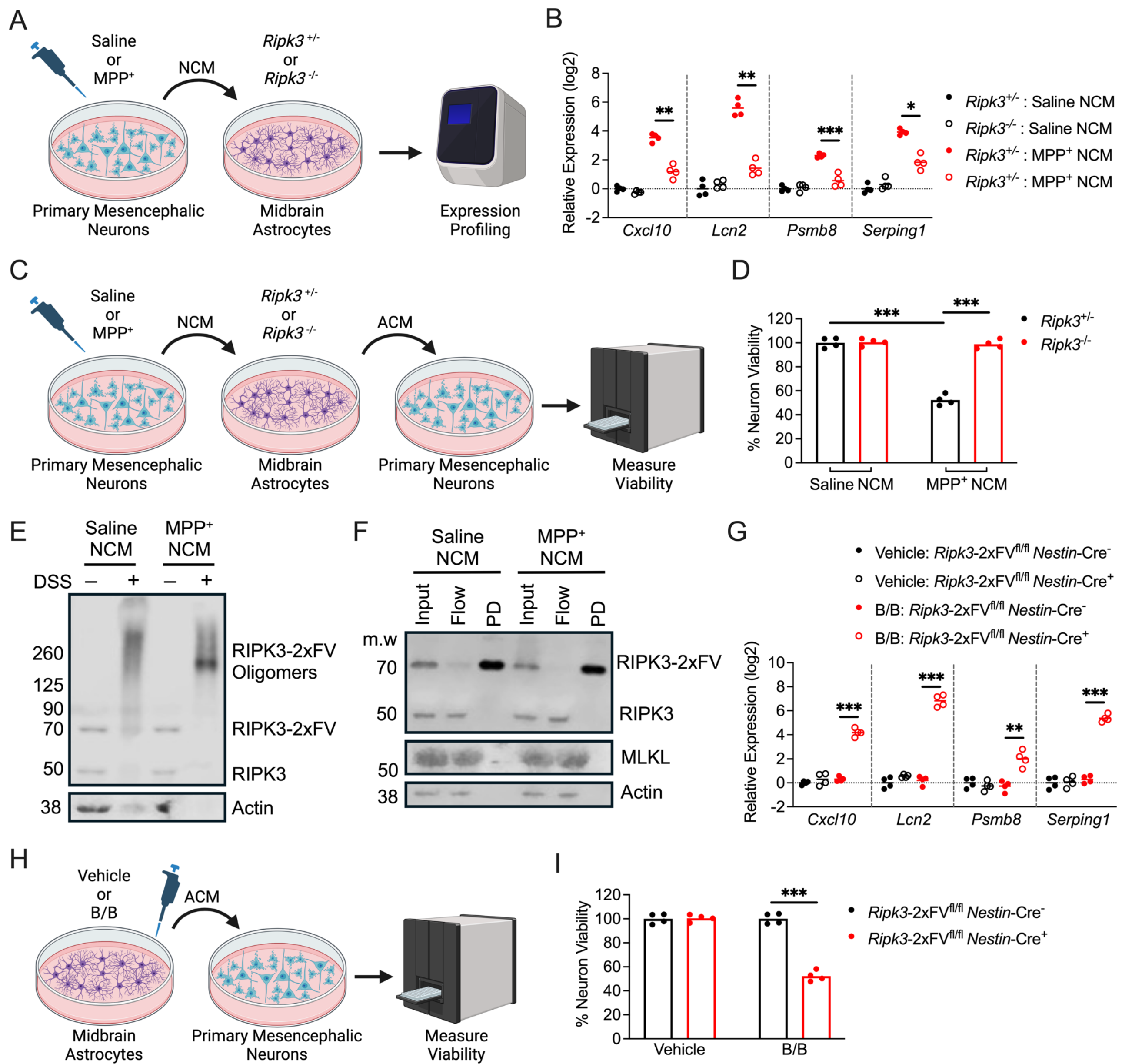

905

906 **Figure 6. *RIPK3 activation is sufficient to induce astrocyte-mediated killing of primary neurons.***

907 **(A)** Schematic of experimental design for DAMP transfer experiments. **(B)** qRT-PCR profiling of

908 indicated genes in astrocytes treated for 24h with clarified NCM supernatants. **(C)** Schematic of

909 experimental design for neurotoxicity assay. **(D)** Cell Titer Glo analysis of neuron viability 24h following

910 treatment with ACM derived from indicated conditions. (**E-F**) Western blot analysis of indicated proteins

911 in astrocytes expressing FLAG-tagged RIPK3 following 24h treatment with NCM and DSS crosslinking

912 (**E**) or bead-mediated FLAG pulldown (**F**). **(G)** qRT-PCR profiling of indicated genes in astrocytes of

913 indicated genotypes treated for 24h with B/B homodimerizer. **(H)** Schematic of experimental design for
914 neurotoxicity assay in which astrocytes expressing (or not) RIPK3-2xFV were treated with B/B
915 homodimerizer or vehicle solution for 24h. Astrocytes were then washed and media replaced for
916 another 24h. ACM was then transferred to WT primary neurons for cell viability measurement. **(I)** Cell
917 Titer Glo analysis of viability in WT neurons 24h following treatment with ACM derived from indicated
918 conditions. N= 4 cultures/per group in all panels. All comparisons via 2-way ANOVA with Sidak's
919 multiple comparison test. *$p<0.05$, **$p < 0.01$, ***$p < 0.001$. **(A, C, H)** were created with Biorender.com.

920

921

922

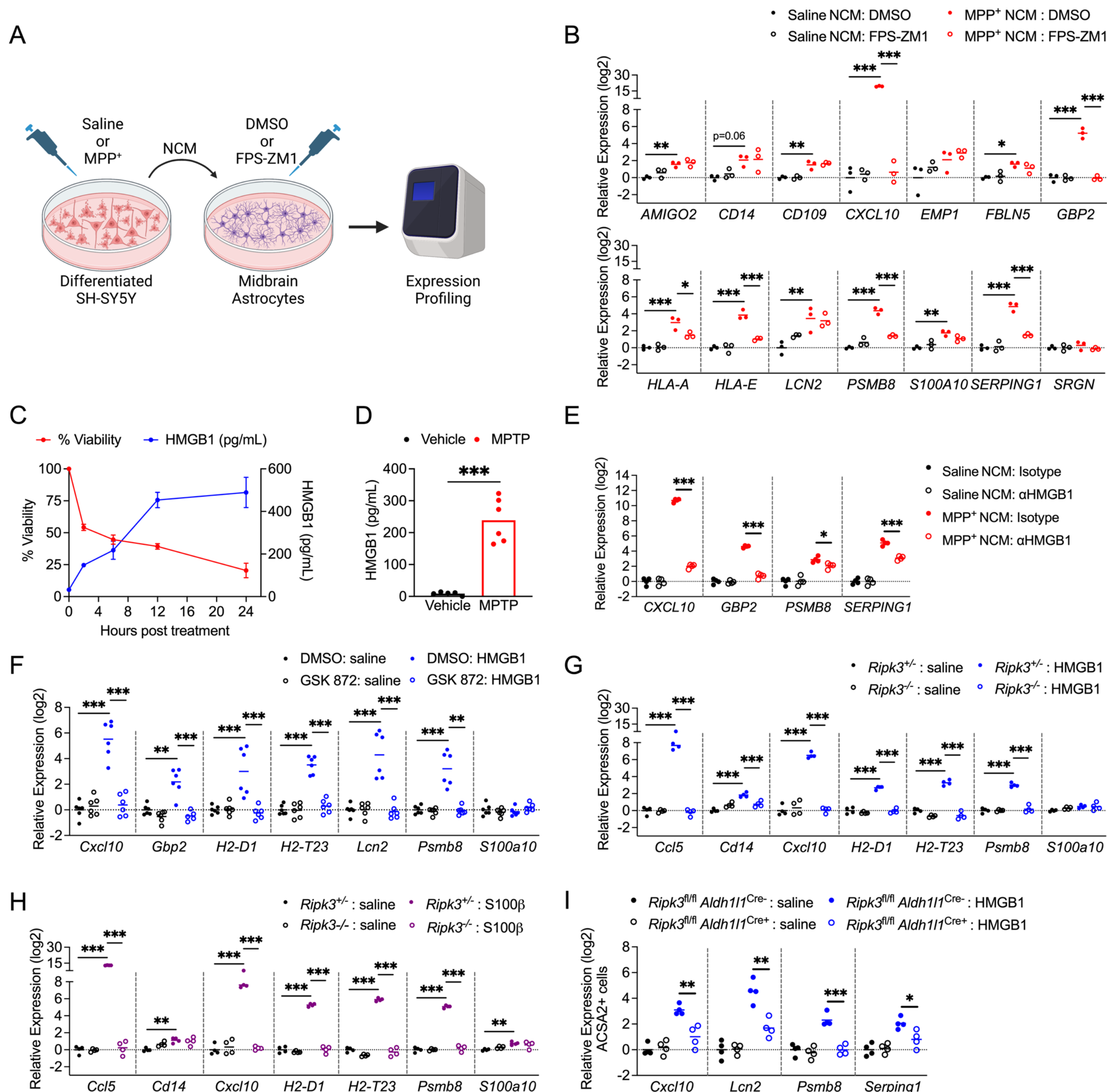

923 **Figure 7. *DAMP signaling via RAGE drives inflammatory activation in midbrain astrocytes.* (A)**
924 Schematic of experimental design for DAMP transfer experiments. Astrocytes were treated with NCM in
925 the presence of FPS-ZM1 or control for 24h prior to qRT-PCR profiling. **(B)** qRT-PCR profiling of
926 indicated genes in astrocytes treated for 24h with NCM derived from indicated conditions**. (C-D)** ELISA
927 analysis of HMGB1 protein levels in supernatants of SH-SY5Y cells treated with MPP^+ **(C)** or midbrain
928 homogenates from WT mice 3 days post-MPTP treatment **(D)** n=4-8 replicates per time point in **(C)**. **(E)**

929 qRT-PCR profiling of indicated genes in human midbrain astrocytes treated for 24h with NCM derived
930 from indicated conditions in the presence of neutralizing antibodies against HMGB1 (1 µg/ml) or an
931 isotype control antibody**. (F-H)** qRT-PCR analysis of indicated genes in WT murine midbrain astrocytes
932 **(F)** or midbrain astrocytes derived from indicated genotypes **(G-H)** 24h following treatment with
933 recombinant HMGB1 **(F-G)** or S100β **(H). (I)** qRT-PCR analysis of indicated genes in ACSA2+
934 astrocytes sorted via MACS from brains of mice 24h following ICV administration of HMGB1 (200ng).
935 N= 3 cultures/group **(B)**, 8 cultures/group for viability data and 2-4 cultures per group for HMGB1
936 expression **(C)**, 5-6 mice/group **(D)**, 6 cultures/group **(E)**, 4 cultures/group **(F-G)**, and 4 mice/group **(H)**.
937 Comparisons via 2-tailed t test **(D)** or 2-way ANOVA with Sidak's multiple comparison test
938 **(B,E,F,G,H,I)**. *p<0.05, **p < 0.01, ***p < 0.001. **(A)** was created with Biorender.com.
939
940

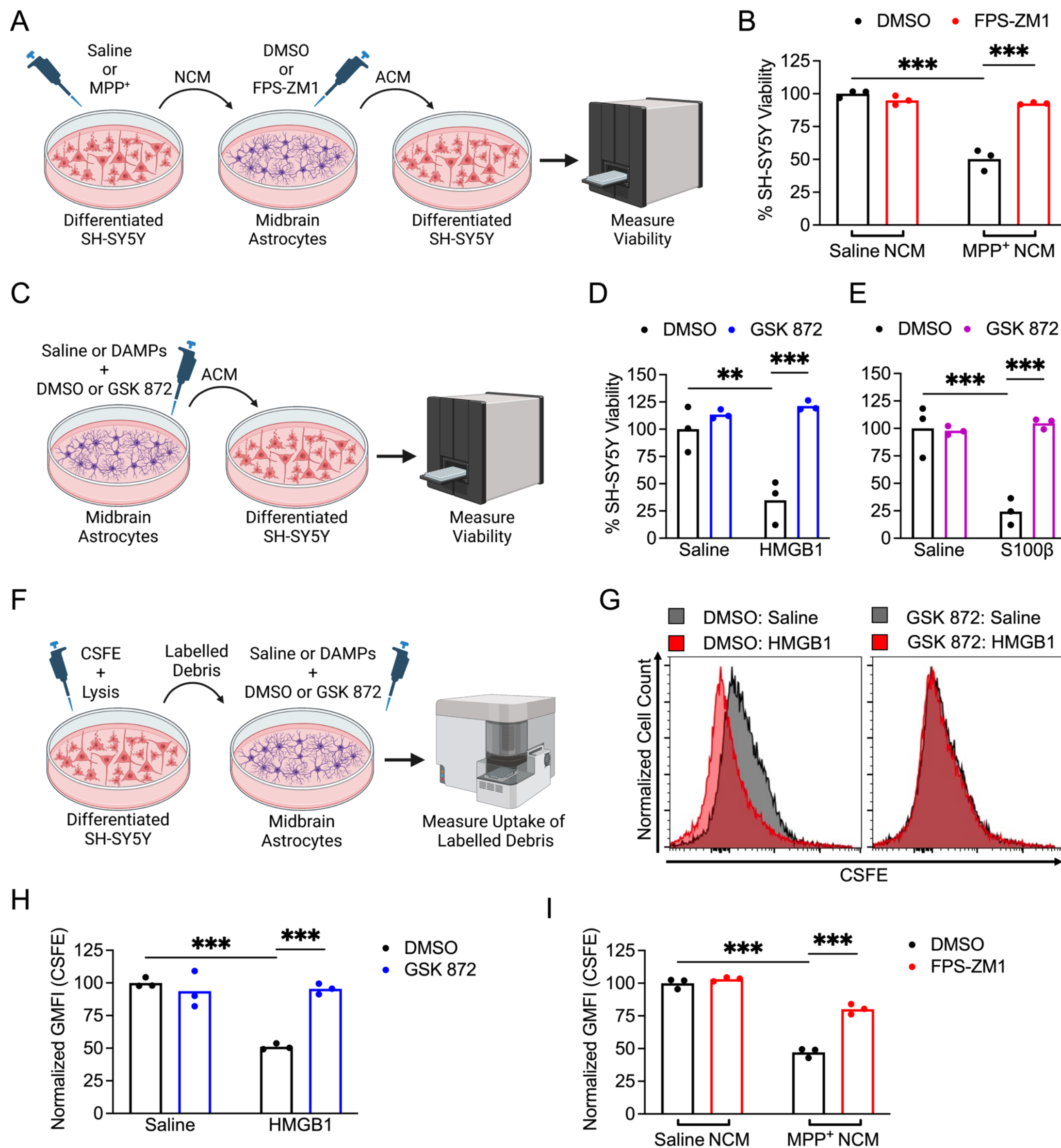

941

942 **Figure 8. *Activation of RIPK3 by DAMP signaling drives pathogenic functional changes in*

943 *midbrain astrocytes.*** **(A)** Schematic of experimental design for neurotoxicity experiments. Astrocytes

944 were treated with NCM in the presence of FPS-ZM1 or control for 24h. ACM was then transferred to

945 fresh SH-SY5Y cells for cell viability measurement. **(B)** Cell Titer Glo analysis of SH-SY5Y viability 24h

946 following treatment with ACM derived from indicated conditions. **(C)** Schematic showing treatment of

947 primary human midbrain astrocytes with recombinant DAMPs for 24h prior to transfer of ACM to SH-

948 SY5Y cultures. **(D)** Cell Titer Glo analysis of SH-SY5Y viability 24h following treatment with ACM

949 derived from indicated conditions**. (F)** Schematic showing generation and transfer of CSFE-labeled

950 neuronal debris to midbrain astrocytes treated with recombinant DAMPs with or without GSK 872.

951 Astrocytes were cultured in the presence of labelled debris for 24h. **(G-H)** Representative histograms

952 **(G)** and quantification of GMFI **(H)** of CSFE signal in astrocytes treated as in **(F). (I)** GMFI of CSFE

953 internalization in astrocytes treated as in **(F)** but with NCM rather than recombinant DAMPs and FPS-

954 ZM1 rather than GSK 872. N= 3 cultures/group in all panels. All comparisons via 2-way ANOVA with

955 Sidak's multiple comparison test. **p < 0.01, ***p < 0.001. **(A, C, F)** were created with Biorender.com.

956